

The Impact of the Three-Dimensional Structure of a Subduction Zone on Time-dependent Crustal Deformation Measured by HR-GNSS

Oluwaseun Idowu Fadugba *¹, Valerie J. Sahakian ¹, Diego Melgar ¹, Arthur Rodgers ², Roey Shimony ¹

¹Department of Earth Sciences, University of Oregon, Eugene, OR, ²Lawrence Livermore National Laboratory, Livermore, CA

Author contributions: *Conceptualization:* O.F., V.J.S., D.M.. *Data Curation:* O.F., V.J.S., D.M., R.S.. *Formal Analysis:* O.F., V.J.S., D.M.. *Funding Acquisition:* V.J.S., D.M.. *Investigation:* All authors. *Methodology:* All authors. *Project Administration:* O.F., V.J.S., D.M.. *Resources:* O.F., V.J.S., D.M., A.R.. *Software:* D.M., A.R.. *Supervision:* V.J.S., D.M., A.R.. *Validation:* O.F., V.J.S., D.M.. *Visualization:* O.F., V.J.S., D.M.. *Writing – original draft:* O.F., V.J.S., D.M.. *Writing – review & editing:* All authors.

Abstract Accurately modeling time-dependent coseismic crustal deformation as observed on high-rate Global Navigation Satellite System (HR-GNSS) lends insight into earthquake source processes and improves local earthquake and tsunami early warning algorithms. Currently, time-dependent crustal deformation modeling relies most frequently on simplified 1D radially symmetric Earth models. However, for shallow subduction zone earthquakes, even low-frequency shaking is likely affected by the many strongly heterogeneous structures such as the subducting slab, mantle wedge, and the overlying crustal structure. We demonstrate that including 3D structure improves the estimation of key features of coseismic HR-GNSS time series, such as the peak ground displacement (PGD), the time to PGD (t_{PGD}), static displacements (SD), and waveform cross-correlation values. We computed synthetic 1D and 3D, 0.25 Hz and 0.5 Hz waveforms at HR-GNSS stations for four M7.3+ earthquakes in Japan using MudPy and SW4, respectively. From these synthetics, we computed intensity-measure residuals between the synthetic and observed GNSS waveforms. Comparing 1D and 3D residuals, we observed that the 3D simulations show better fits to the PGD and SD in the observed waveforms than the 1D simulations for both 0.25 Hz and 0.5 Hz simulations. We find that the reduction in PGD residuals in the 3D simulations is a combined effect of both shallow and deep 3D structures; hence incorporating only the upper 30 km of 3D structure will still improve the fit to the observed PGD values. Our results demonstrate that 3D simulations significantly improve models of GNSS waveform characteristics and will not only help understand the underlying processes, but also improve local tsunami warning.

Production Editor:
Gareth Funning
Handling Editor:
Mathilde Radiguet
Copy & Layout Editor:
Hannah F. Mark

Received:
April 23, 2023
Accepted:
March 10, 2024
Published:
May 3, 2024

1 Introduction

Real-time high-rate Global Navigation Satellite System (HR-GNSS) are key observational data for kinematic slip inversions (e.g., Ozawa et al., 2011; Melgar et al., 2016) that provide an important lens into large earthquake rupture physics (e.g., Melgar and Bock, 2015), as well as for real-time applications in Earthquake and Tsunami Early Warning (EEW/TEW) (e.g., Sahakian et al., 2019a). Kinematic slip inversions, traditionally based on broadband seismograms and strong motion data, are used for rapid and retrospective seismological studies to understand earthquake complexities through finite fault models, source time function and directivity, etc. (e.g., Ide, 2007; Goldberg et al., 2022). HR-GNSS waveforms are an important contribution to these models to constrain the time-dependent, low-frequency deformation of the Earth's surface. In the resulting finite fault model, this yields not only slip on the fault, but information about the rupture kinematics for each sub-fault, thus providing both spatial and temporal distribution of slip on a more granular level (e.g., Melgar and Bock, 2015; Melgar et al., 2020b). When per-

formed in real-time, rapid kinematic source models are an important component of TEW approaches (hence, better rapid local tsunami modeling). HR-GNSS data also provide crucial constraints for rapid earthquake magnitude estimation, in particular for large magnitude earthquakes as the displacement metrics they provide do not saturate, unlike displacement obtained from broadband seismograms (e.g., Bock et al., 2011; Melgar et al., 2016; Sahakian et al., 2019a) and the displacement obtained from twice-integrated strong motion records do not resolve observed static offset measured by GNSS, even when high-pass filters are applied (Goldberg et al., 2021). In addition to constraining rapid finite-fault inversions for local TEW, the peak ground displacement (PGD) and time to reach peak ground displacement (t_{PGD}) as recorded by HR-GNSS can play a key role in discriminating tsunami earthquakes (TsEs) from non-TsEs (Sahakian et al., 2019a).

Static and kinematic slip inversion models using displacement time series from HR-GNSS waveforms are routinely performed using simplified 1D radially symmetric Earth models, by determining the displacement from each subfault with a 1D Green's function (Melgar and Bock, 2015), as it is oft assumed that three-

*Corresponding author: ofadugba@uoregon.edu

dimensional heterogeneities play a smaller role in the low-frequency content of waveforms than for high-frequency seismic data. However, the availability of high-rate GNSS data and the need to resolve earthquake and wave propagation details with higher frequencies and shorter wavelengths exposes the inadequacy of 1D models for analysis of large earthquake ruptures. Many studies using 1D structure observed some delays and unmodeled features in the HR-GNSS waveforms from the 2011 moment magnitude (M) 9.0 Tohoku-Oki earthquake (Yue and Lay, 2011; Melgar and Bock, 2015), as well as other earthquakes (e.g., Delouis et al., 2010).

Subduction zones present unique three-dimensional challenges that may not be well-captured by 1D models. Due to complex geometry, the resultant onshore deformation and shaking from megathrust events is likely affected by many strongly heterogeneous structures such as the slab, the wedge, the overlying crustal structure, etc. However, current models of time-dependent crustal deformation using HR-GNSS displacement waveforms, or low-frequency shaking, typically use Green's function approaches and 1D Earth structure, omitting the effects of the 3D Earth structure on the wave path, hence on the observed waveforms. In this work, we present results comparing 1D to 3D models of time-dependent crustal deformation and find that three-dimensional effects are non-negligible, and should be an important component of kinematic modeling. Although the importance of including 3D structure to model strong-motion data is well-established in the literature (i.e., Vidale and Helmberger, 1988; Olsen, 2000; Hartzell et al., 2010; Rodgers et al., 2019), this study provides quantitative estimates on the influence of neglecting 3D effects and specifically investigates the application to modeling time-dependent low frequency crustal deformation, such as that measured by HR-GNSS, still used for a variety of seismological applications.

2 Background

Previous studies have contributed to the advancement of slip models in a 3D Earth structure (e.g., Wald and Graves, 2001; Williams and Wallace, 2015; Tung and Masterlark, 2018) and show that material contrasts between continental crust and oceanic slabs have a large effect on recovering static coseismic displacements, slow slip events, slip distributions and tsunami behavior in elastic models. For example, Tung and Masterlark (2018) show that the inclusion of heterogeneous crustal structure can remove nonrealistic slip artifacts in slip distributions and reduce the misfit in large seafloor displacement that contributes to prediction error of tsunami amplitudes. Williams and Wallace (2015) also show a better fit to the observed GNSS displacements by computing Green's functions using a realistically varying elastic properties with a finite element method (Aagaard et al., 2013). Hearn and Burgmann (2005) show similar effects in strike-slip settings, comparing 1D structure and homogeneous half space models. They find an improvement in the estimation of the moment and centroid depth from GNSS measurements by incor-

porating earth's layered elastic structure in the slip inversion. This reduces the disparity between the geodetic and seismic moment estimates for large strike-slip earthquakes and suggests that time-dependent crustal deformation should be affected by depth-dependent elasticity. Langer et al. (2022) use a synthetic model of sedimentary basin to investigate the impact of 3-D elastic structure on forward models of co-seismic surface deformation and suggest the use of a layered velocity structure in static slip inversion in regions with sedimentary basins. Langer et al. (2019) show the importance of including topography in coseismic deformation modeling.

Together, these advances show that both static and dynamic (time-dependent) crustal deformation suffer from "path effects" in the same way that high-frequency ground motions as measured on strong-motion instruments do. Path effects are a common source of uncertainty in ground motion models that focus on the effects of seismic waves' path on higher frequency intensity measures (Baltay et al., 2017; Kotha et al., 2020; Landwehr et al., 2016; Zhang et al., 2022; Sahakian et al., 2019b; Kuehn and Abrahamson, 2019), and it stands to reason that they likely play a role in low to moderate frequencies (~1 Hz, that of HR-GNSS and time-dependent crustal deformation) as well.

Better modeling of time-dependent, coseismic crustal deformation can make significant contributions to improving our understanding of underlying large earthquake source processes, as well as improving warning and rapid response systems overall (Wirth et al., 2022). In this work, we show a comparison of 1D vs. 3D deterministic HR-GNSS waveforms for events in Japan to show the impact of 3D structure on accurately modeling GNSS waveforms. We choose Japan to test our hypotheses, as its seismicity, HR-GNSS recordings, and knowledge of 1D and 3D structures are ideal for our purposes. Japan has an excellent GNSS Network (~1178 stations), a good number of M7.3+ earthquakes, and both 1D and 3D velocity models (Fig. 1). We will show that the effects of including 3D structures is most important in improving the PGD at all hypocentral distances and static displacements (SD) residual values at hypocentral distances greater than 350-400 km.

3 Data and Methods

We generate 1D and 3D low-frequency synthetic GNSS waveforms of M7.3+ megathrust earthquakes in Japan and compare the 1D and 3D synthetics with the observed GNSS waveforms using several waveform intensity measures. We also test different rupture models for some of the earthquakes to investigate the effect of rupture model on the intensity measures.

3.1 Data

We focus on four M7.3+ megathrust earthquakes in Japan with good rupture models: 2011 M7.9 Ibaraki, 2011 M7.4 Iwate, 2011A M7.3 Miyagi and 2003 M8.3 Tokachi 2003 (Fig. 1; Table 1). We did not include the 2011 M9.0 Tohoku-Oki earthquake due to computational

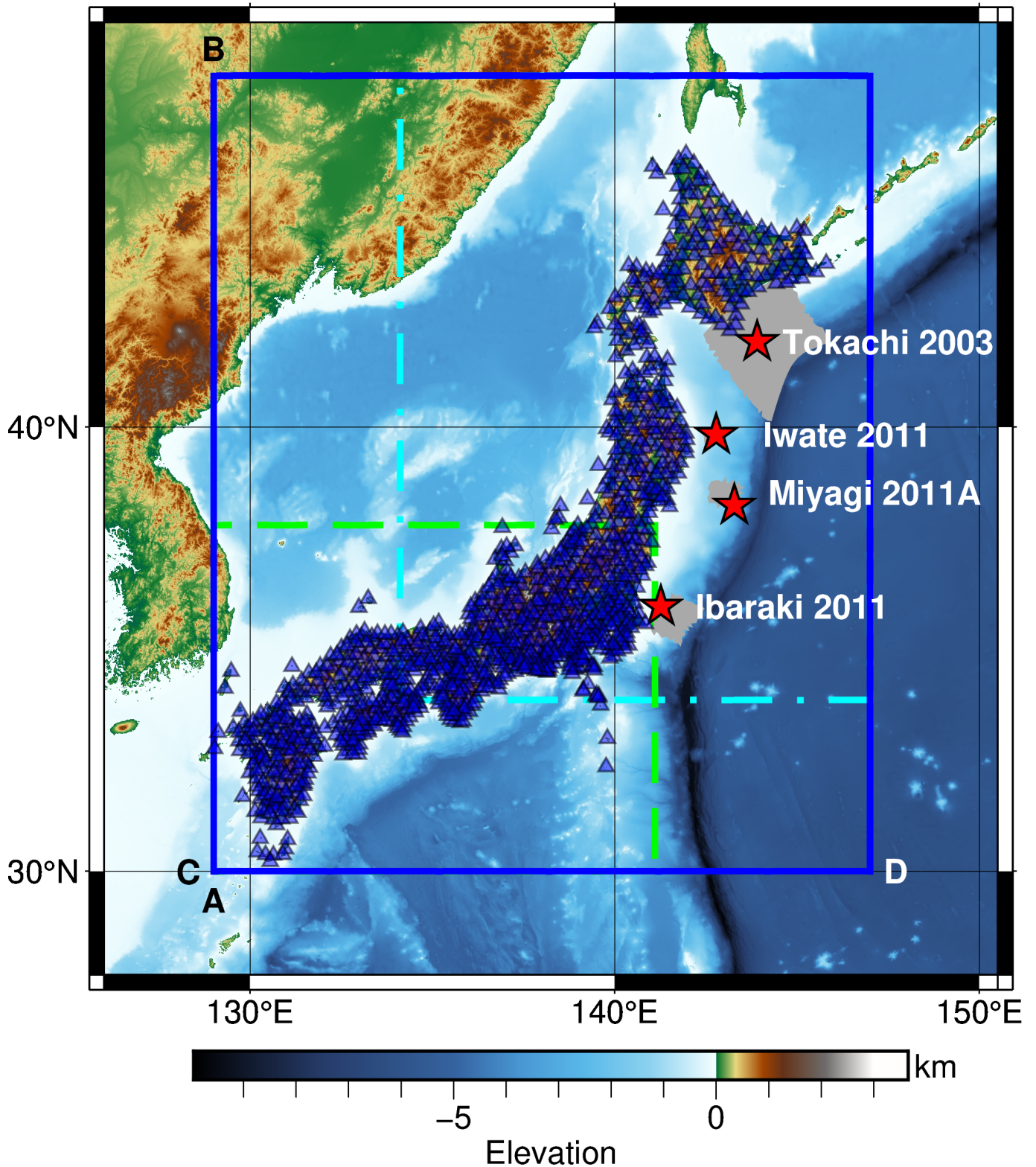


Figure 1 Study region around Japan with topography and bathymetry showing the HR-GNSS stations (blue triangles) used to observe and model at least one earthquake ($SNR \geq 3$). The figure also shows the four earthquake epicenters (red stars) used in this study and their published ruptures (the dark gray regions show the subfaults associated with the earthquakes, see Table 1). The lines show the 3D Japan Integrated Velocity Structure Model (Koketsu et al., 2008, 2009) domains: West region (green dashed line), East region (cyan dashed-dotted line) and Combined region (blue solid line). Edges AB and CD show the profile lines of the 3D Japan Integrated Velocity Structure Model presented in Fig. 4.

cost of the 3D simulations, but we expect similar conclusions with the M7.3+ earthquakes used in this study. We

used the 1Hz GNSS waveforms from Ruhl et al. (2018), obtained using the Precise Point Processing approach

and, from these, determine total horizontal displacement waveform $T(t)$ using Equation 1:

$$T(t) = \sqrt{N(t)^2 + E(t)^2} \quad (1)$$

We focused on the total horizontal displacement as the vertical displacement measurement in HR-GNSS are less accurate due to the distribution of GNSS satellites and generally assigned an error of about 3-5 times that of the horizontal (e.g., Geng et al., 2018; Melgar et al., 2020a). The use of $T(t)$ ensures that the more significant error in the vertical displacement compared to the horizontal displacement measurements is not influencing the 1D to 3D comparison, thus avoiding the misfit due to noise as opposed to the effect of the 3D structure.

3.2 1D Simulation Using FakeQuakes/MudPy

We used the FakeQuakes and MudPy software (Melgar et al., 2016) to generate 1D synthetic waveforms using a 1D velocity model in two steps. FakeQuakes first produces stochastic kinematic rupture models using a published rupture model as a mean slip model following the approach of Goldberg and Melgar (2020).

We give a brief description of the FakeQuakes methods, but we refer readers to Melgar et al. (2016) for more details of the method and validations. FakeQuakes generates slip distributions from the perturbations around a known slip model given a target magnitude or mean slip distribution and a prescribed fault geometry. To do so, FakeQuakes uses a von Karman correlation function to obtain the covariance matrix using correlation lengths between the subfaults associated with the rupture. The tunable parameters are the Hurst exponent and standard deviation of the slip on each subfault. It then determines the length and width of the portion of the prescribed fault geometry that will participate in the rupture using the Blaser et al. (2010) relationship which is based on the magnitude of the earthquake. It uses a lognormal probability density function approach to introduce some variability in the fault dimension. We set H to 0.4 based on Melgar and Hayes (2019) and used a uniform standard deviation of the slip (s) value of 0.9 for all subfaults. FakeQuakes then uses the Karhunen-Loève (K-L) expansion (LeVeque et al., 2016) to determine several nonnegative slip distributions by linear combinations of the eigenmodes of a lognormal covariance matrix that are sampled from a probability density function with the desired covariance matrix. Linear combinations of more modes redistributes slip over the fault model; we set the number of modes in the K-L expansion to 72 to obtain short variability of the slip distribution necessary for kinetic rupture modeling. For example, mode 0 is roughly the alterations of the mean slip based on the lognormal covariance matrix.

To avoid an unrealistically large amount of slip, we set the limit on the peak value of slip to 40 m so that any realizations that exceed 40 m are discarded. Finally, FakeQuakes follows Graves and Pitarka (2010, 2014) to obtain the kinematic parameters of the rupture such as the rupture speed and duration of slip (rise time). The rupture speed is a factor of the shear-wave speed at the

subfault depth, and rise time based on the slip at each subfault. The factor of the shear-wave speed is 0.4 in the shallow region (<10 km) and 0.8 for the deeper region (>15 km), and a linear transition in rupture speed is applied between 10 and 15 km depth. The local slip-rate function of each fault is based on the Dreger slip-rate function (Mena et al., 2010) with a fallout rate of 4.

We then use MudPy to generate displacement time series from the kinematic rupture models with an FK Green's function approach (Zhu and Rivera, 2002) using a 1D layered Earth. We used a sampling interval of 1 s and a total duration of 512 s. FakeQuakes/MudPy requires the fault and rupture models, 1D velocity model and the GNSS station locations as input parameters.

We used the Slab2.0 model (Hayes, 2018) to create a fault geometry mesh for the Japan Trench using Gmsh, a 3-D finite element mesh generator (Geuzaine and Remacle, 2009). Details of the fault files are described in the Supplementary Material (S1). We focused on the Kuril region of Japan where the M7.3+ megathrust earthquakes used in this study are located. We use the published rupture models for the four megathrust earthquakes as input mean slip distributions for FakeQuakes (Table 1). For the Ibaraki 2011 earthquake, we used the Kubo et al. (2013) rupture model (henceforth referred to as SRCMOD) and Zheng et al. (2020, henceforth referred to as Zheng) rupture model. For the Miyagi 2011A earthquake, we used the Hayes (2017, henceforth referred to as Hayes) and Zheng rupture models. For the Tokachi 2003 earthquake, we used models from Koketsu et al. (2004), Yamanaka and Kikuchi (2003), Yagi (2004) (henceforth referred to as SRCMOD, SRCMOD2 and SRCMOD3, respectively) and Hayes rupture models. We used only the Zheng rupture model for Iwate 2011 earthquake (Table 1).

The geometries of the published rupture models are planar and do not coincide with the geometry of Japan trench from Slab2.0, so, we project the slip in the rupture model for each earthquake onto the fault geometry (Fig. S2 Fadugba et al., 2023). Specifically, we project both the subfault locations of the rupture model and the centroid of the mesh of the fault geometry on a 2D plane with a strike of 210 and a dip value of 20 based on the fault geometry's general strike and dip values. We then performed linear interpolation to evaluate the strike- and dip-slip amounts from the rupture model at the mesh locations.

With FakeQuakes, we generated 100 realizations of the published rupture models using the published model as a mean model. Figure 2 shows the mean rupture model (SRCMOD) for the Ibaraki 2011 earthquake (Kubo et al., 2013) and three examples of the 100 FakeQuakes ruptures realizations from the mean rupture model. FQ Model 3 is an end-member example of a rupture model with a different slip pattern compared with the mean slip model, but with similar moment release and falling within the prescribed uncertainties of the mean slip model. The mean rupture models and examples of FakeQuakes ruptures of the other earthquakes used in this study are in the Supplementary material (Fig. S3-S4).

We adopted the 6-layer crustal velocity structure of

| SN | Event Name | Origin Time (UTC) | Latitude (°) | Longitude (°) | Depth (km) | Moment magnitude (M) | Number of GNSS Stations (SNR \geq 3) | Rupture Models and corresponding references |
|----|--------------|---------------------|--------------|---------------|------------|----------------------|--|---|
| 1 | Ibaraki 2011 | 2011-03-11T06:15:34 | 36.1083 | 141.2653 | 43.2 | 7.9 | 737 | SRCMOD (Kubo et al., 2013) |
| 2 | Iwate 2011 | 2011-03-11T06:08:53 | 39.8390 | 142.7815 | 31.7 | 7.4 | 271 | Zheng (Zheng et al., 2020) |
| 3 | Miyagi 2011A | 2011-03-09T02:45:12 | 38.3285 | 143.2798 | 8.3 | 7.3 | 240 | Hayes (Hayes, 2017) |
| 4 | Tokachi 2003 | 2003-09-25T19:50:06 | 41.7750 | 143.9040 | 27.0 | 8.3 | 236 | Hayes (Hayes, 2017) |

Table 1 Earthquakes used in this study and the corresponding rupture models. SN: Source Number.

Mean Rupture Model and Example FQ MODEls (Ibaraki 2011 SRCMOD)

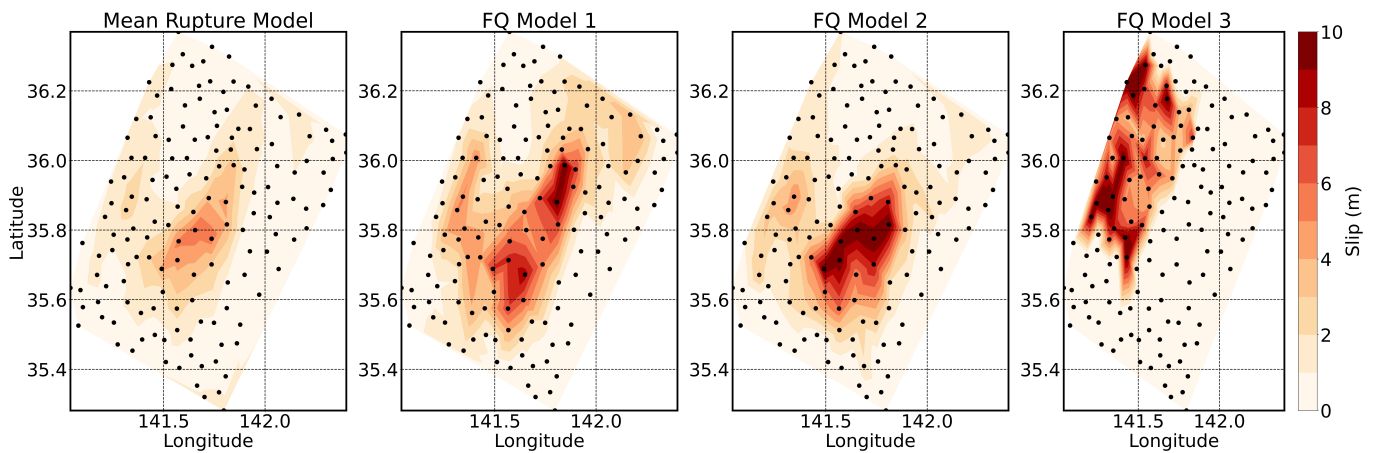


Figure 2 Mean Rupture model (SRCMOD) for Ibaraki 2011 earthquake (Kubo et al., 2013) and three examples of the 100 FakeQuakes (FQ) ruptures realizations from the mean rupture model. The color indicates the amount of slip per subfault, and the black dots signify the center of each subfault. The slip is greater overall in the FakeQuake models compared to the mean slip model in the top left to conserve the moment release in response to the change in rigidity at the subfault locations compared to the one used to generate the mean slip model. FQ Model 3 is an end-member example of a rupture model with different slip pattern compared with the mean slip model, but with similar moment release.

Hayes (2017) for all the earthquakes for its simplicity and the ease to set it up in our 1D and 3D simulations (Fig. 3). We used the isotropic Preliminary Reference Earth Model (PREM) from 40 to 200 km depth (Dziewon-ski and Anderson, 1981). There are other well-known 1D velocity models for Japan that could be used (e.g., Ueno et al., 2002; Hayes, 2017; Laske et al., 2013). The Japan Meteorological Agency (JMA) uses a 1D velocity model (Ueno et al., 2002) to locate earthquakes in Japan. However, the model has a series of 500 m thick layers which are less practical to setup for our 3D simulations, and we aim for consistency between the 1D and 3D simulations.

The earthquakes were recorded on a total of 1178 GNSS stations. However, to reduce computation time, we only simulate waveforms for stations with an observed total horizontal displacement signal-to-noise ratio (SNR, Equation 2) larger than or equal to 3, thus reducing the number of stations for each earthquake simulation (Table 1). SNR is defined by

$$SNR = \frac{\sigma_{signal}}{\sigma_{noise}} \quad (2)$$

where σ_{signal} is the standard deviation of 120s of

recorded ground shaking after the P-wave arrival time while σ_{noise} is the standard deviation of 10s recordings before the P-wave arrival time. P-wave arrival time is defined as the origin time plus an approximate P-wave travel time (i.e., hypocentral distance between HR-GNSS station and rupture model hypocenter, divided by 6.5 km/s).

To understand the impact of the source rupture model on our synthetic waveforms, we investigated the effect of rupture models in the 1D simulations using two rupture models for the 2011 M7.9 Ibaraki and 2011A M7.3 Miyagi earthquakes and three rupture models for 2003 M8.3 Tokachi earthquake, and compare their residuals.

3.3 SW4 3D Simulations

Our 3D synthetic waveforms were computed using SW4 2.01 (Pettersson and Sjögreen, 2012, 2015; Sjögreen and Pettersson, 2011; Pettersson and Sjögreen, 2017) published under the GPL2 license. SW4 solves the seismic wave equations in displacement formulation using a 4th order accurate summation-by-parts finite differ-

1D Velocity Model (Hayes, 2017)

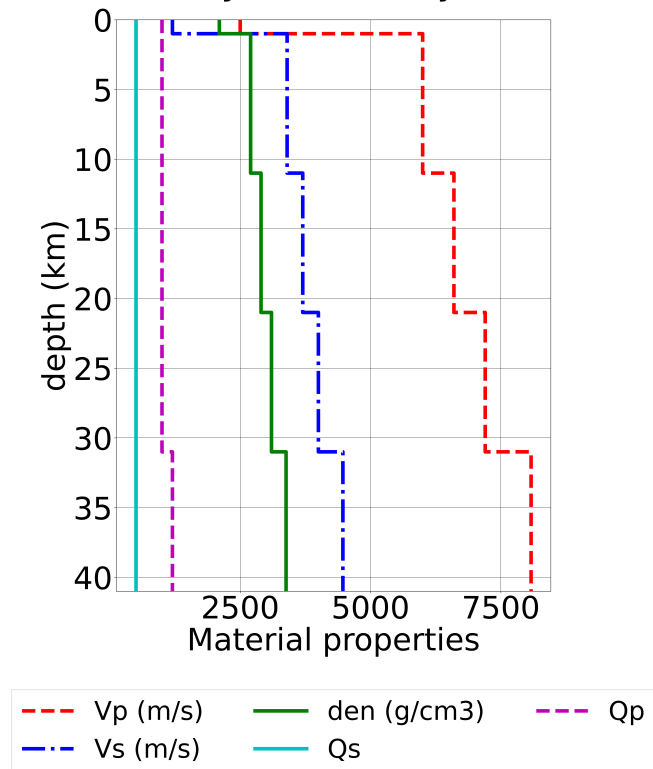


Figure 3 1D velocity model of Japan (Hayes, 2017) showing the P-wave velocity profile (red dashed line), S-wave velocity profile (blue dashed line), density profile (green solid line), and P- and S-wave quality factors (Qp and Qs) profiles (purple dashed line and cyan solid line, respectively). We used this 1D velocity model for the upper 40 km and the PREM model (Dziewonski and Anderson, 1981) from 40 km up to 200 km.

ence method, a 3D model of velocity structure, and a domain geometry that includes both topography and bathymetry. Because this process is so computationally intensive, similar to the large-scale SW4 simulations of earthquakes on the Hayward Fault (Rodgers et al., 2020), we generated simulations for all four events at both 0.25 and 0.5 Hz, to compare with observations and understand if characteristic intensity measures such as PGD require information from higher frequencies.

We used the 3D Japan Integrated Velocity Structure Model (Koketsu et al., 2008, 2009) which includes topography and bathymetry data from the ETOPO1 1 arc-minute global relief model (N.O.A.A. National Geophysical Data Center, 2009) spanning a lateral extent of latitude from 30° to 47° North (~2040 km) and longitude from 129° to 147° (~1440 km) East. We convert the 3D velocity structure from an ASCII text file to a raster file format (rfile), as it is more effective for smoothly varying 3D heterogeneous structure (Fig. 4; Petersson and Sjögren, 2017). An rfile is a binary structured grid format, and it is the most efficient and realistic method to input 3D velocity structure to SW4, hence more suitable for this study. The 3D Japan Integrated Velocity Structure Model (JIVSM) comprises 23 layers, each with constant P- and S-wave velocities (V_p and V_s), density (ρ) and P- and S-wave quality factors (Qp and Qs) (Table S1). The

3D structure is given in two overlapping sections (East and West Japan, Fig. 1), but were combined to create the unified 3D velocity model of Japan by extrapolating the top of each layer to regions outside the 3D structure regions following the OpenSWPC methodology (Maeda et al., 2017). The resulting rfile has 5 blocks with increasing grid spacing with depth: grid spacing of 200 m at the top to 1000 m at the bottom of the rfile. The grid sizes of rfile are independent of the grid sizes in the computational domain (Petersson and Sjögren, 2017). The minimum grid size in the computational grid depends on the desired maximum frequency. Details of the rfile are in the Supplementary Material (S2).

Our domain depths extended from the surface (topography and bathymetry) to a maximum depth of 200 km. The maximum achievable frequency (f_{max}) is dependent on the grid size of the domain, as well as the minimum shear wave speed, as described by:

$$f_{max} = \frac{\min V_s}{PPW \times h} \quad (3)$$

SW4 allows user to set the P- and S-wave minimum velocity values in the simulations using the global material command, thus replacing the velocity layer whose V_p and V_s are smaller than threshold values with the threshold values. We used 8 Points Per Wavelength (PPW) in the simulations and the minimum shear wave speed ($\min V_s$) value of 1200 m/s based on the average V_s value in the upper 400 m in the 3D velocity model (Equation 3; Petersson and Sjögren, 2017). We set the minimum P-wave velocity value in the simulations to 2500 m/s. To generate 3D synthetic waveforms with a maximum frequency of 0.25 and 0.5 Hz, we used a minimum grid spacing (h) of 600 and 300 m, respectively. We used a curvilinear mesh from the surface (topography and bathymetry) to 30-km depth with a grid spacing of 300 m and used Cartesian mesh from 30 km downwards. Within the Cartesian mesh, we applied grid refinement at 75 km depth to reduce the computational resources required for these simulations. Our grid spacing increased with depth and the associated increasing $\min V_s$: 300 m and 600m grid spacing for the 30-75 km and 75 – 200 km depth range, respectively. For the 0.50 Hz SW4 simulations, we varied the lateral extent of the 3D domain geometry depending on location of each earthquakes (Fig. S5) to limit the maximum memory required by the simulations to ~4TB (Supplementary Material S3). We compared only the intensity measures from the common stations between the 1D and 3D simulations.

For the 0.25 Hz simulations, we selected two of the 100 rupture models from FakeQuakes for each earthquake and read them into SW4 format using the Standard Rupture Format version 2.0 source representations (Graves, 2014). We used only one rupture model for the 0.5 Hz simulations due to their high computational cost.

3.4 Comparing 1D vs. 3D Synthetic Waveforms

We compare the 1D and 3D synthetics with the observed GNSS waveforms using the total horizontal component

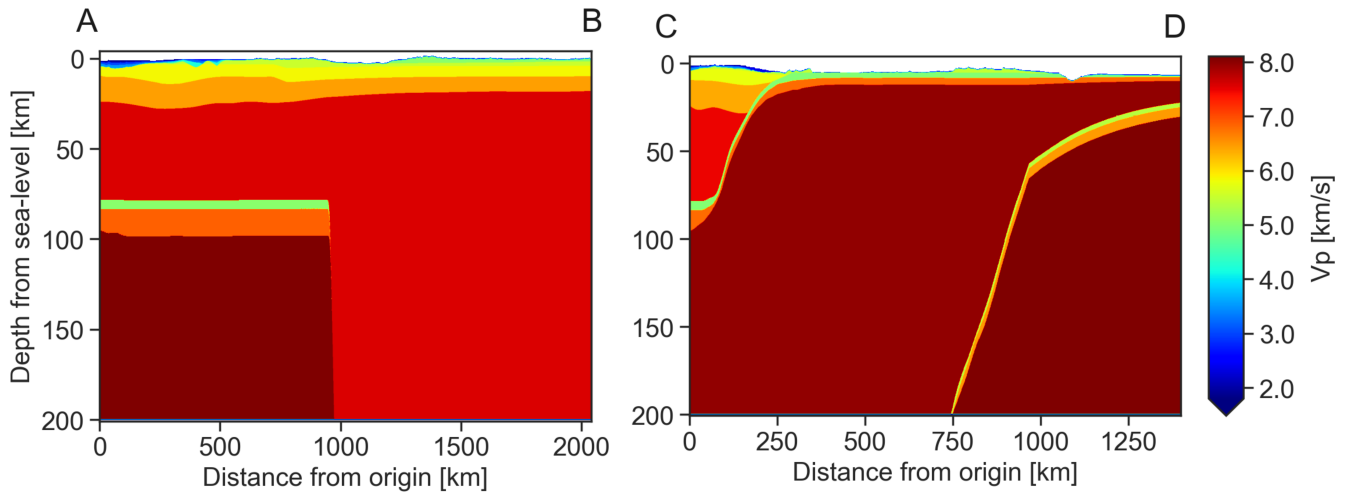


Figure 4 3D Japan Integrated Velocity Structure Model (JIVSM, Koketsu et al., 2008, 2009) shown for the AB and CD profile lines marked in Figure 1. The profile CD shows the geometries of the two subducting slabs and both profile lines best show the heterogenous velocity structure in the upper 30 km depth of the 3D velocity structure.

waveforms. In addition to wiggle-to-wiggle comparisons via waveform cross-correlation with time-shifting for both 1D and 3D synthetics, we also model the average behavior of important features of the observed waveforms over many realizations from the mean rupture models. We measure the goodness of fit by comparing the misfits of the total horizontal waveform synthetic and observed waveforms using waveform intensity measures such as the PGD as defined in Goldberg et al. (2021), t_{PGD} , and SD residuals, each described in Figure 5.

We then determine the residuals for the PGD and SD intensity measures using the equation

$$\delta_{ij,PGD} = \ln \left(\frac{PGD_{obs}}{PGD_{syn}} \right) \quad (4)$$

A residual (δ_{ij}) of 0 corresponds to perfect equivalence between observed and synthetic values, while residual values of 0.5 and 1.0 signify that the observed value is 1.6x and 2.7x the synthetic values, respectively. For the t_{PGD} residuals, we use the difference between the time it takes to reach the PGD for observed and synthetic waveforms:

$$\delta_{ij,t_{PGD}} = t_{PGD,obs} - t_{PGD,syn} \quad (5)$$

Cross-correlation values inherently compare the fit between observed and synthetic waveforms.

We investigate the variation of each intensity measure with distance by binning the intensity measures with respect to the hypocentral distance, the distance between rupture model hypocenter and the HR-GNSS station. Each intensity measure is defined for a paired station and rupture model (Equations 4, 5), and we combined the residuals from all stations and rupture models into a single dataset and binned with respect to the hypocentral distance. The residuals in each bin are plotted using box and whisker plots. These combine the minimum and maximum values with the quartiles into one useful graph. It consists of a horizontal line, drawn according

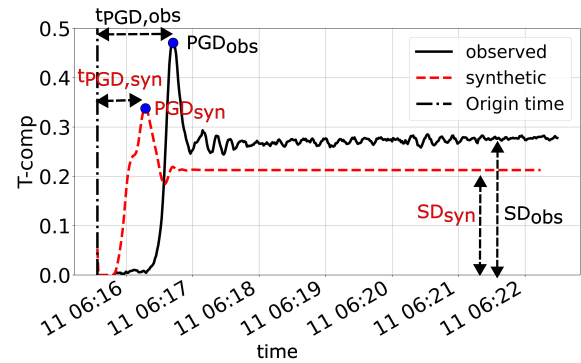


Figure 5 Schematic representation of the definitions of the intensity measure used in comparing the total horizontal waveform synthetic (“syn”) and observed (“obs”) waveforms. Black solid and red dashed lines are the observed and synthetic waveforms, respectively. The blue dots show the Peak Ground Displacement (PGD) for the observed and synthetic waveforms and their corresponding time to reach the PGD (t_{PGD}). The figure also shows the definition of static displacement (SD). The amplitude and time axes values in this figure are arbitrary.

to scale, and a box drawn from the lower (Q_1) to upper (Q_3) quartile with a vertical line marking the median. The minimum and maximum values of the whisker correspond to the smallest and largest data points from the dataset that fall within 1.5 times the inter-quartile range ($IQR = Q_3 - Q_1$). Outliers are observed data points that are more than 1.5 times the IQR below Q_1 or more than 1.5 times the IQR above Q_3 . For a normal distribution, the IQR contains 50% of the population and 1.5 of the IQR contains about 99%. We removed the outliers outside the whiskers to improve readability.

4 Results and Discussions

4.1 Comparing 1D and 3D Residuals

First, as a control, we study the impacts of varying only the source model by investigating the residuals using only 1D velocity structure, with different published rupture models. The PGD residuals ($\delta_{ij,PGD}$, Equation 4) for all the earthquakes in the 1D simulations increase with distance but are generally below 2 (Fig. 6). On each boxplot, residuals for each model are shown as patterned box and whisker plots, including blue circle patterns (SRCMOD), orange grid (SRMOD 2), light blue circled (SRCMOD 3), gray slanted (Hayes), and orange diamonds (Zheng). The red horizontal line represents the zero residual line. In the 1D simulations, PGD residuals do not change significantly with distance when we used different rupture models for the same earthquake (e.g., Hayes, SRCMOD, SRCMOD2, and SRCMOD3 for the 2003 Tokachi earthquake). Therefore, any deviations in the PGD residual for the same rupture model in 3D simulations are most likely due to the 3D Earth structure. We observed that the PGD residuals for MudPy 1D Zheng model is lower than that of the MudPy 1D SRCMOD model, but we will show later that the residuals for 3D velocity models are still lower than the corresponding 1D models.

We evaluated a possible bias in the choice of the 1D velocity model since the mean rupture models (Table 1) are derived from 1D crustal models by other researchers (e.g., Zheng et al., 2020). We have shown that the choice of 1D velocity model, even though different from the source models' 1D model, do not affect the conclusions and the PGD residuals in the 1D simulations will still very different from the 3D simulations (Fig. S6). We performed 1D simulations for the Ibaraki 2011 earthquake using the SRCMOD mean rupture model but using 1D velocity models used by Koketsu et al. (2004) and Zheng et al. (2020). We compared the PGD residuals of the resulting waveforms using these 1D velocity models with respect to the observed waveforms. The comparison plot shows that the PGD residuals using these additional 1D velocity models are different in some sense but are not significantly different compared to the trend of residuals observed for the 3D simulations shown later. Therefore, any deviation from the PGD residual in the 1D simulations is due to the path rather than the choice of the 1D velocity model.

The effect of this is exemplified in the comparison of the observed and the MudPy 1D and SW4 0.25 Hz and 0.5 Hz synthetic waveforms at stations 0041 and 0043 for the Ibaraki 2011 earthquake for one of the 100 FakeQuake ruptures using the SRCMOD mean rupture model (Kubo et al., 2013) (Fig. 7). The MudPy 1D waveforms are very simple, but the SW4 waveforms better capture the variability in the observed waveforms. Specifically, the 3D waveforms and in particular the higher frequency 3D waveforms better capture the dynamic shaking in addition to the static offset observed at each station. This includes capturing a commonly observed dynamic overshoot, such as that observed in the North component of stations 0041 and 0043 for the Ibaraki earthquake, at

~60s (Fig. 7).

In a map view, we further show the effect of the 3D structure by overlaying the magnitude of velocity waveforms at the surface as a function of time on a topography/bathymetry map to highlight the spatial and temporal variation of the wavefront as it propagates (Fig. 8). The wavefronts appear spherical up to about 120s (Fig. 8E) and reveal a strong energy propagating SE away from the land. At 140s (Fig. 8F), the wavefronts show evidence of a waveguide on the low-velocity wedge as the energy propagates at a lower velocity within the wedge area exemplifying the effect of the 3D structure. The extent of the packet of energy coincides with the geometry of the Japan trench. The packet of energy within the wedge continues to propagate northward as the wavefront propagates through Japan. At 200s (Fig. 8H), the wavefronts reveal a basin effect in the Nankai and Sagami Troughs located SW of the Japan Trench and in the Sea of Japan. The wavefront also shows a waveguide phenomenon in the low-velocity wedge of the Nankai Trough and the packet of energy propagates westward at a slower velocity in the wedge even though the earthquake is located on the Japan Trench. From 270s onwards (Fig. 8J), the wavefront traveling northward through the wedge appears to bifurcate into the bay region towards Tomakomai and the other energy continues northward within the wedge. The observed waveguiding in the shallow slabs and the wave amplification in the Nankai and Sagami Troughs area show that lower frequencies still demonstrate non-negligible path effects, which may be important to the seismic hazard of Japan. Furthermore, this demonstrates that three-dimensional effects are important to include in kinematic slip models, as they may currently be wrapped into the source model.

This observation is distinctly different from the subduction guided waves observed from deep earthquakes on the subducting Pacific plate in Japan (Furumura and Kennett, 2005), as well as other regions globally (Furumura and Kennett, 1998; Furumura and Singh, 2002; Sahakian et al., 2018; Mann and Abers, 2019). In Japan, Furumura and Kennett (2005) observed an anomalously large intensity on the eastern seaboard of northern Japan from deep-seated earthquakes and the waveforms show a low-frequency ($f < 0.25$ Hz) onset for both P and S waves, followed by large, high frequency ($f > 2$ Hz) later arrivals with a long coda. They did not observe the characteristics of frequency-selective wave propagation for subduction zone earthquakes with hypocenter depth less than 185 km. They explained this observation as arising from scattering of seismic waves by an elongated scatterer parallel to the plate margin. Despite the similarity in the phenomenon, the Ibaraki 2011 earthquake shown in Figure 8 has a hypocenter depth of 43.2 km and the maximum frequency in the waveforms is 0.25 Hz. We observed that the intense shaking is concentrated within the shelf regions and is bounded by the trench geometry. This shows that the shaking may be due to waveguide phenomena within the low-velocity wedge. Indeed, in other subduction zones such as the Hikurangi, the sedimentary wedge is demonstrated to act as a waveguide, increasing shaking

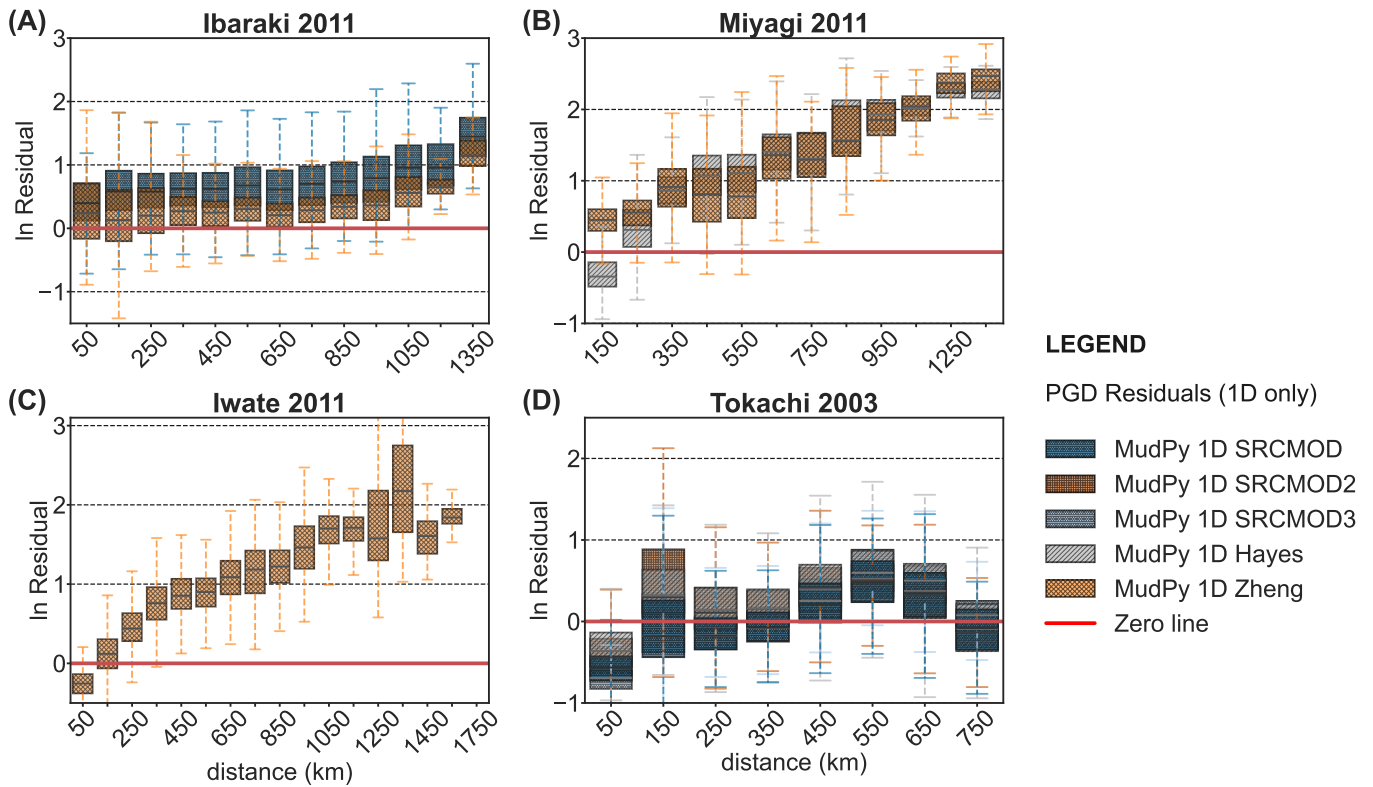


Figure 6 PGD Residuals using only the 1D velocity model, demonstrating the effects of varying solely the source model for all the four earthquakes using all the 100 random realizations of the mean rupture model. A, B and D show the effect of rupture models on the PGD residuals from 1D simulations using Ibaraki 2011, Miyagi 2011A and Tokachi 2003 earthquakes. On each boxplot, residuals for each model are shown as patterned box and whisker plots, including blue boxplot with circle patterns (SRCMOD), orange boxplot with grid patterns (SRMOD 2), light blue boxplot with circled patterns (SRCMOD 3), gray boxplot slanted patterns (Hayes), and orange boxplot with diamonds patterns (Zheng). The red horizontal line represents the zero residual line.

and dynamic stresses for longer period ground motions (Wallace et al., 2017; Kaneko et al., 2019). A more detailed examination of the waveguide is beyond the scope of this paper.

The PGD, t_{PGD} , SD residuals, and cross correlation residual maps for the Ibaraki 2011 earthquake showing the spatial variation of the residuals are in the supplementary materials (Fig. S8). The PGD residual is generally near zero and positive, but $< \ln(1)$. We observed the residual is more positive near the coastal region of the Nankai Trough. However, an isolated zone with negative PGD residuals is observed near Kanazawa at the Japan Sea Margin. The t_{PGD} residual is generally positive and below 50 s, but slightly negative on the Japan Sea Margin. It is also noteworthy that the static displacement residuals are generally near zero but become more variable farther away from the hypocenter, especially toward SW Japan. The cross-correlation values between the SW4 3D waveforms and the observed waveforms show a decay in values with distance but are generally above 0.7.

4.2 Residual Analyses

Comparing 1D and 3D residuals, we observed that the 3D simulations residuals are clearly near zero (closer to the observed intensity measures) than the 1D residuals at all distances, except for the Tokachi earthquake

(Fig. 9 and S9). The distributions of the intensity measures show improved fitting to the observed waveforms in the 3D simulations. These results suggest that accounting for path-specific 3D structure improves the fit to the observed waveforms compared to the 1D simulations. The width of the residual distributions is to some degree controlled by the parameters used to vary the random slip model realizations upon a mean model as described in the methods; however, there is not necessarily a one-to-one relationship between these parameters (such as h) and the width of the residual distributions here. Furthermore, the difference between 1D and 3D residuals is significantly greater than the difference between residuals for any given models of an event (Figure 6), demonstrating that the structure has a greater effect than any potential bias due to the source model selection.

For a more quantitative aggregate comparison, we determine the difference between the magnitude of the 3D median residuals compared to 1D median residuals for each residual boxplot (Equation 6, Fig. 10). We compute the difference as:

$$\delta_{|3D|-|1D|} = |\delta_{3D}| - |\delta_{1D}| \quad (6)$$

where $|\delta_{1D}|$ and $|\delta_{3D}|$ are absolute values of the 1D and 3D median residuals, respectively. The median residual difference measures how much the 3D median residual is closer to the zero value (i.e., fits the observed

Ibaraki 2011 (SRCMOD Rupt 5)

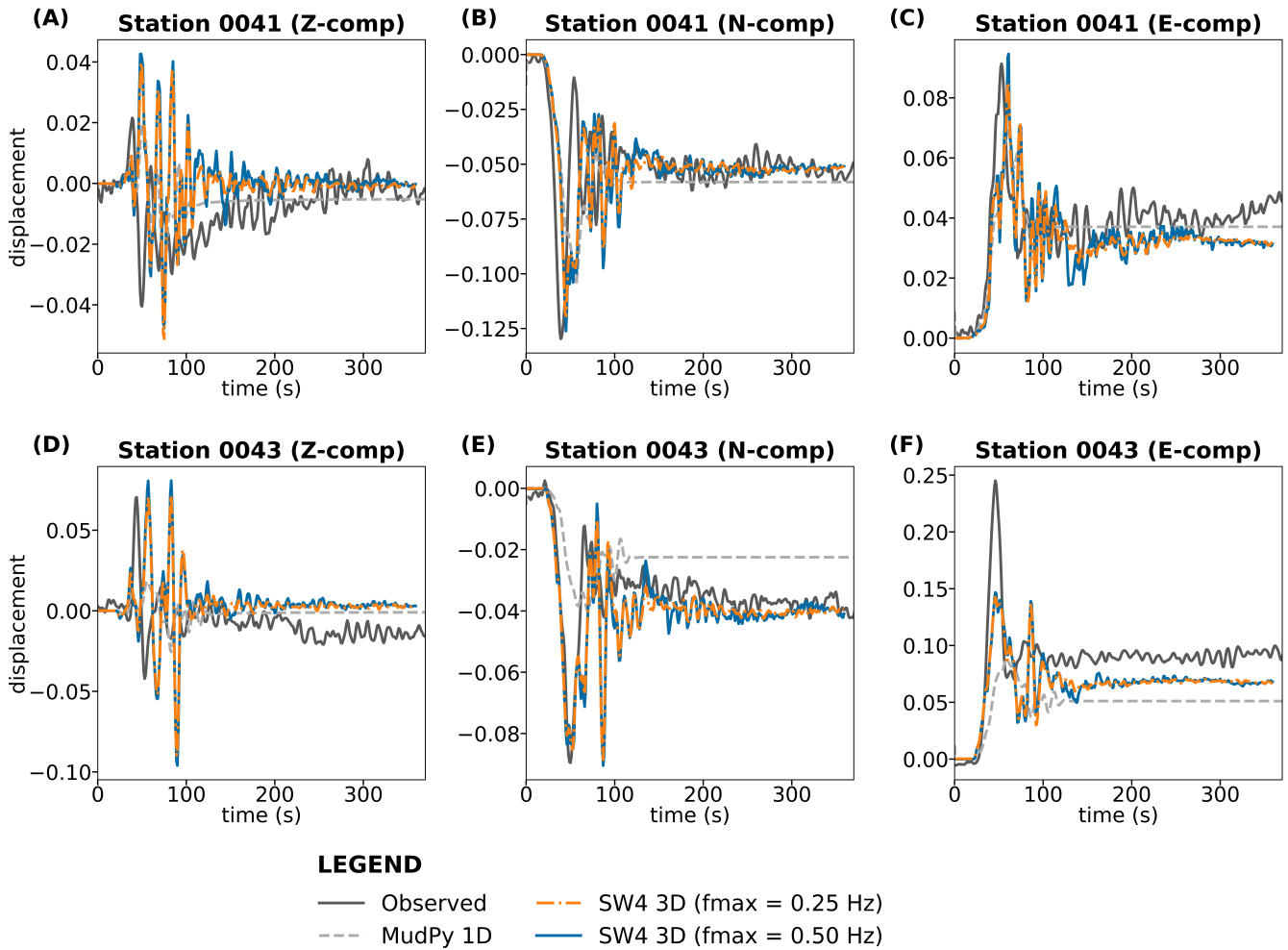


Figure 7 Comparing the observed (dark gray solid line) and three synthetic waveforms: MudPy 1D (dashed gray line), SW4 0.25 Hz (dashed-dotted orange line) and 0.50 Hz (blue solid line) waveforms at stations 0041 and 0043, respectively. The MudPy 1D waveforms are very simple, but the SW4 waveforms better capture the variability in the observed waveforms. The observed waveforms were shifted back by 20 s to fit the synthetic waveforms. The figure shows the vertical (Z-comp) and the horizontal components (N-comp and E-comp) of the waveforms.

waveform) than the 1D simulations. A negative value of median residual difference shows that 3D simulations fit better to the observed intensity measure than the 1D simulations and vice versa. Note that this convention is different for the median residual difference for the cross-correlation values because a positive median residual difference for the cross-correlation shows that the 3D simulations fit the observed waveforms better.

To determine if the 1D and 3D residuals are statistically different from each other (i.e., come from different distributions), we perform Kolmogorov-Smirnov (K-S) tests (Kolmogorov, 1933; Smirnov, 1948) on the 1D and 3D residuals for each earthquake. Two distributions are significantly different when the statistical value (KS-stat) is above a critical value which is a function of the number of samples of each distribution, and when the p-value is below the significance level of 0.05.

Considering the variation of the median residual of the intensity measures with distance, 3D simulations consistently have lower PGD median residuals

(Fig. 10A) for all simulations with statistical significance (Fig. 10B), except for Tokachi 2003 (Fig. 10A). The t_{PGD} median residuals are consistently lower in the 3D simulations, generally between 250 and 700 km hypocentral distance except for the Ibaraki 2011 earthquake (Fig. 10C). The static-displacement median residuals are similar up to about 400 or 500 km (i.e., near zero), but the 3D simulations fit the observed static displacement better at longer distances (i.e., negative) (Fig. 10E). The cross-correlation median values are slightly higher in the 3D simulations, especially above distances of about 300 km, excepting the Ibaraki 2011 SRCMOD earthquake (Fig. 10G); however, we have no explanation for why this particular model shows lower cross-correlations other than that it may be related to the source inversion parameters.

The plots of the p-value with distance for all the earthquakes show that the 1D vs 3D intensity measure residuals vary with distance for all simulations (Fig. 10). Specifically, the K-S tests show that the distributions of

Surface Magnitude Velocity for Ibaraki 2011 (SRCMOD Rupture 5)

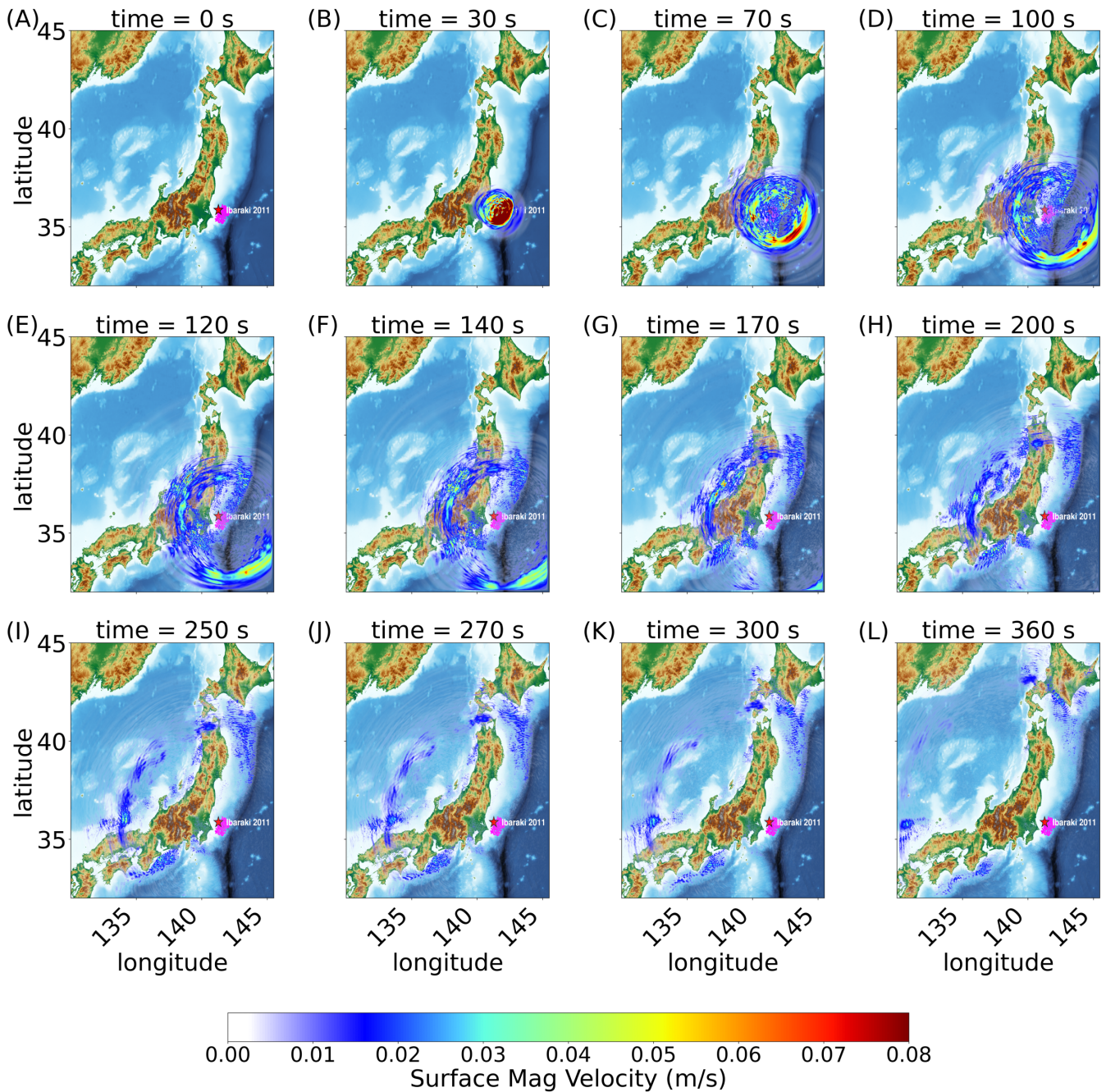


Figure 8 Waveform propagation of Ibaraki 2011 earthquake using rupture 5 of the 100 FakeQuakes random realizations of the SRCMOD mean rupture model (Kubo et al., 2013), showing the effect of 3D velocity structure. The maximum frequency of the simulation is 0.25 Hz. The rupturing subfaults are shown as pink grid cells, and hypocenter as a star. Color bar shows the surface magnitude velocity in m/s.

the PGD residuals in the 1D and 3D simulations are significantly different for all simulations up to hypocentral distance of 1000 km, and below 700 km for the Miyagi 2011 simulations (Fig. 10B). The t_{PGD} residual distributions are significantly different below 600 km distance, except for Ibaraki 2011 and Tokachi 2003 earthquakes below 400 km, which corresponds to the distance range where there is a better fit in PGD residuals for the 3D simulation (Fig. 10D). For both PGD and t_{PGD} residuals, the numbers of samples are generally smaller where the

distributions are not significantly different. Conversely, the p-value plots for the static displacement and cross correlation show similar distributions between the 1D and 3D residuals (Fig. 10F and H).

The observed consistent overall increase in 1D and 3D residuals with distance may be because the source rupture model was derived with a 1D Green’s function. The general trends in the PGD residuals show the 1D and 3D synthetic amplitudes generally decay faster than the observed amplitudes with distance, suggesting the

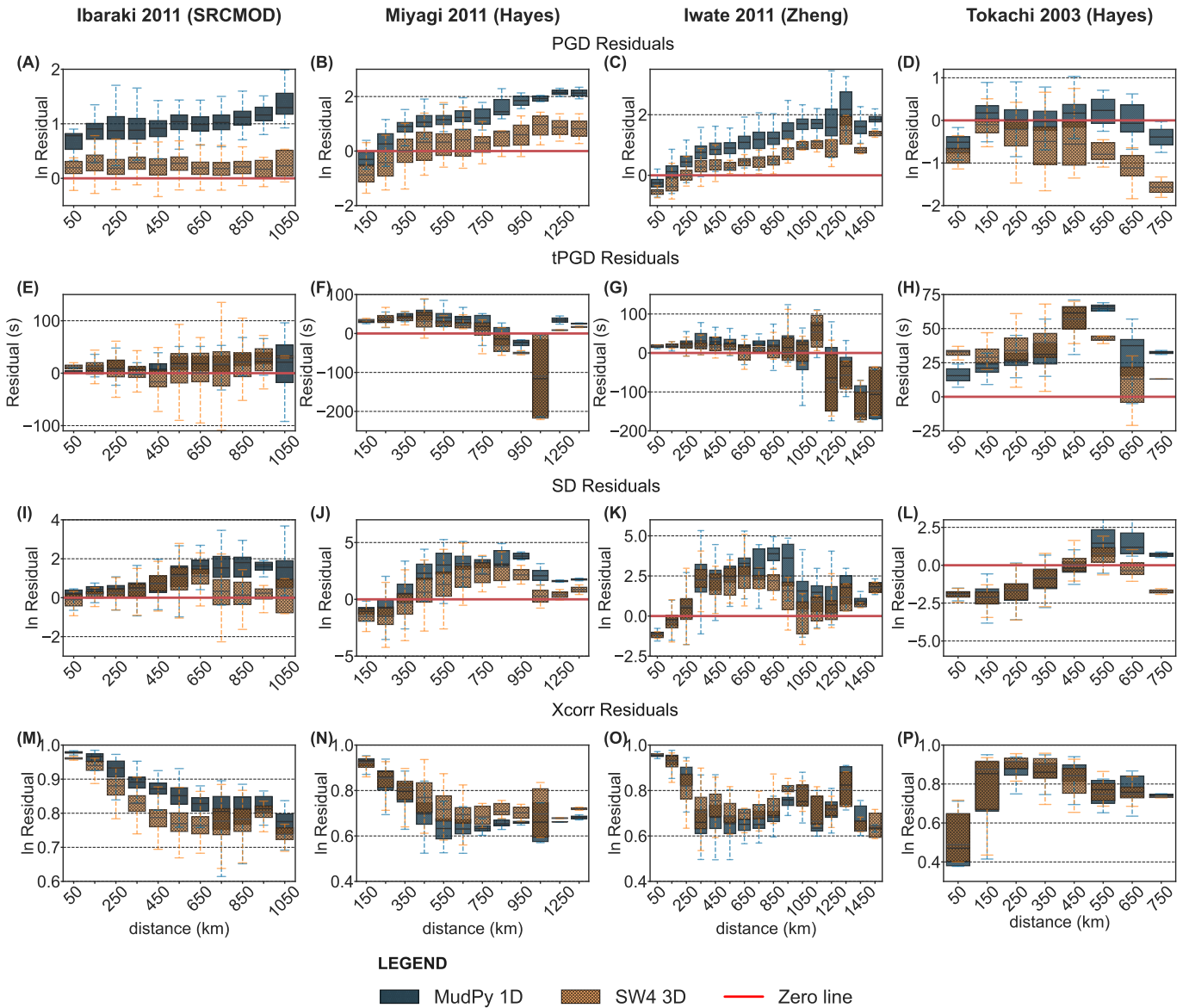


Figure 9 Comparing MudPy 1D vs SW4 3D residuals between the synthetic to observed GNSS waveforms for Ibaraki 2011 (SRCMOD), Miyagi 2011 (Hayes), Iwate 2011 (Zheng) and Tokachi 2003 (Hayes rupture model) with $f_{max} = 0.25$ Hz. (A-D) PGD residuals, (E-H) t_{PGD} (s) residuals, (I-L) static displacement residuals and (M-P) cross correlation values. We compare only the residuals of two corresponding rupture models in the MudPy and SW4 synthetic simulations. The blue boxplots with circle hatched filling represents the MudPy 1D residuals while the orange boxplot (diamond hatch style) represents the SW4 3D simulation. The red horizontal line represents the zero residual line.

variation in attenuation values within a layer unit in the 3D earth structure. Evaluation of the effect of the 1D velocity-derived rupture model and possible variation of attenuation within a layer on the general trend is beyond the scope of this study.

4.3 General Intensity Measure Residuals for Each Earthquake

The intensity measures for each simulation without considering the variation with distance show that the 1D vs. 3D residual distributions are significantly different for all simulations and there is a general reduction in the median residual values (hence, a better fit) in the 3D simulations compared to 1D simulations (Fig. 11).

Of greatest significance, we observed that the PGD residuals in the 3D simulations are smaller by about 0.4

-0.6 units compared to 1D simulations for all simulations, except for Tokachi 2003 (Hayes and SRCMOD3) models. Also, the t_{PGD} in the 3D simulations, in general, better fit the observed than 1D simulations by about 4 seconds, except for Ibaraki 2011 (Zheng) and Tokachi 2003 earthquake simulations. There is a slight reduction in the median static displacement residuals in the 3D simulations except for Ibaraki 2011 (Zheng) and Miyagi 2011 (Hayes) simulations. The 3D simulations generally have higher median cross-correlation values than 1D simulations, up to about 0.03. These results demonstrate that 3D structure plays a large, and statistically significant, role in accurately modeling the PGD and SD, as well as time-dependent characteristics of displacement time series (Fig. 11).

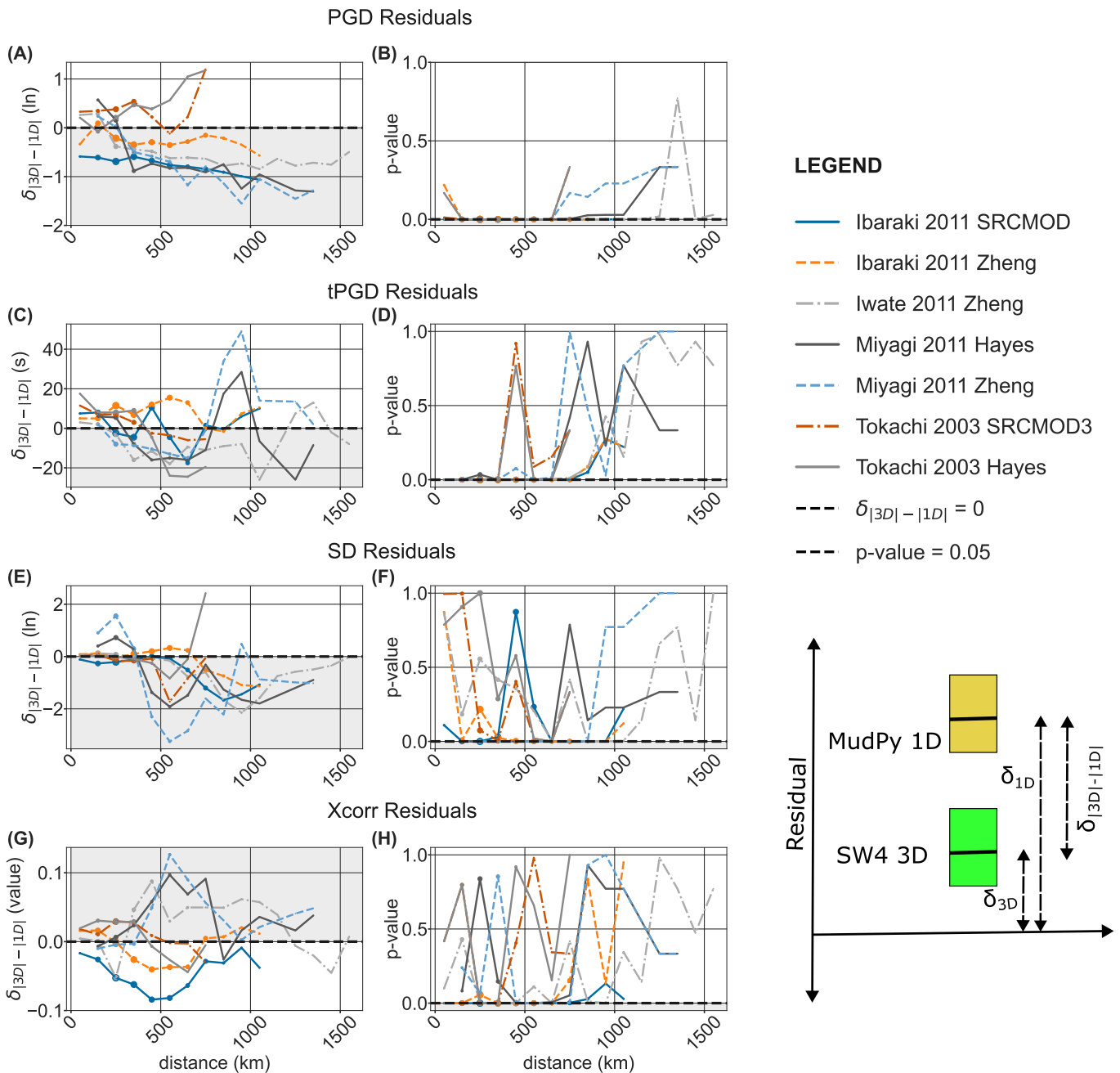


Figure 10 Median residual difference and the P-value for the PGD, t_{PGD} , SD residuals and cross correlation values for all the simulations. Blue solid lines: Ibaraki 2011 SRCMOD, orange dashed lines: Ibaraki 2011 Zheng, gray dashed-dotted line: Iwate 2011 Zheng, Black solid lines: Miyagi 2011 Hayes, blue dashed lines: Miyagi 2011 Zheng, orange dashed-dotted lines: Tokachi 2003 SRCMO3, gray solid lines: Tokachi 2003 Hayes simulations. The gray shaded regions in (A), (C), (E) and (G) represent regions where “3D fits better than 1D” while the white regions represent “1D fits better than 3D”. The gray shaded regions in (B), (D), (F) and (H) represent regions where 1D and 3D residuals are statistically different from each other (i.e., come from different distributions) while the white shaded regions represent regions where 1D and 3D are from the same distribution. The bottom right schematic is a visual representation of the meaning of the mean residual difference.

4.4 Effect of 3D Structure in the Upper 0-30 km

To understand if a well-constrained shallow structure plays a larger role than deeper structure in accurately modeling time-dependent crustal deformation from mid-crustal earthquakes, we tested the effect of 3D structure in the upper 0-30 km on our simulations using the Ibaraki 2011 and Miyagi 2011 earthquakes as case studies. The Ibaraki 2011 earthquake is located at 43.2 km which is below the upper 0-30 km, while the Miyagi

earthquake has a focal depth of 8.3 km, so the earthquake is within the 0-30 km structure (Fig. 1 and 12). We used the upper 0-30 km of the 3D structure because it is the depth region where we observed the most lateral structural heterogeneity.

To do this, we created another rfile for a 3D velocity model involving only the upper 0-30 km depth of the unified 3D velocity model of Japan, which is an extrapolated version of the 3D Japan Integrated Velocity Structure Model (Koketsu et al., 2008, 2009). The SW4 simu-

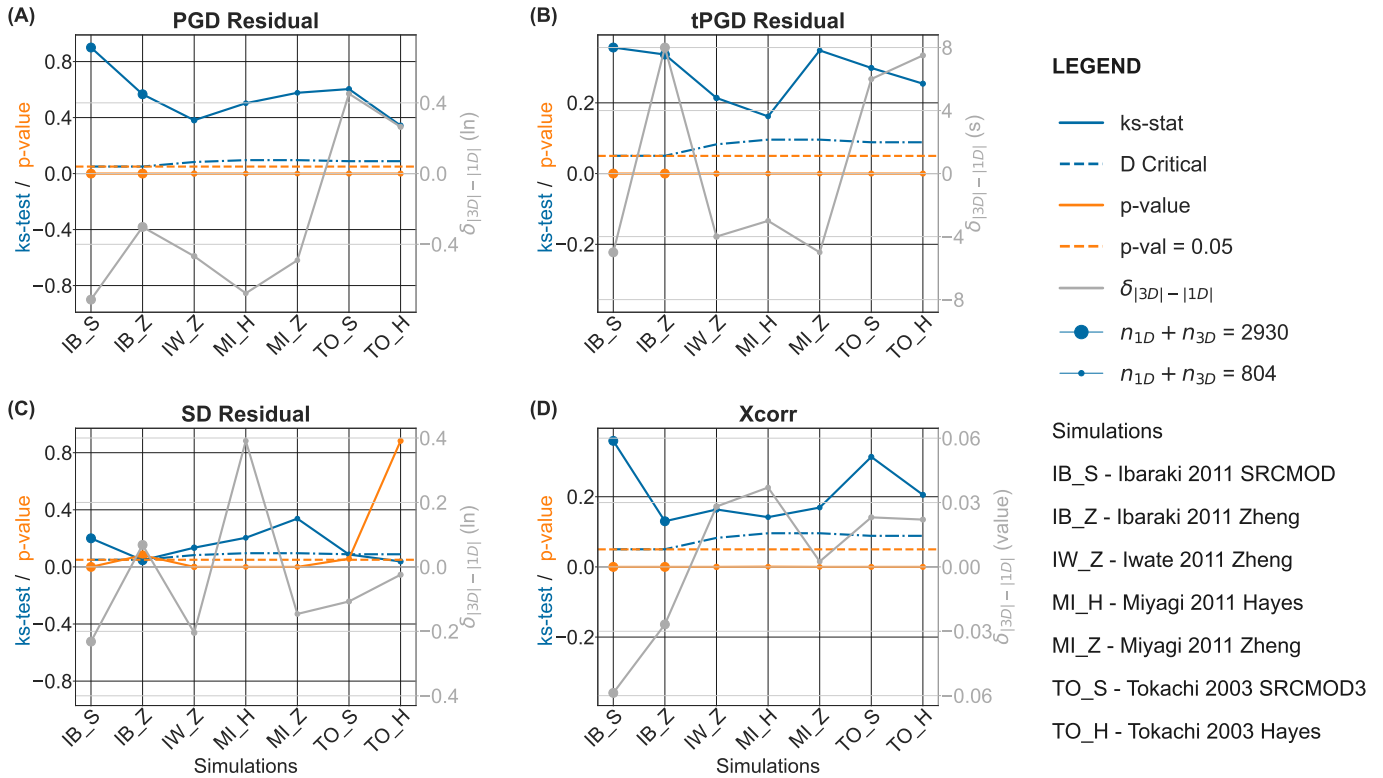


Figure 11 K-S test results and median residual difference between entire MudPy 1D and SW4 3D residual distributions for all simulations. The points are sized by the population size in that bin. Blue solid lines represent the K-S statistic value, blue dash-dotted lines represent the critical value, orange solid lines represent the p value, orange dashed lines represent the p value line of 0.05, and the gray solid line represents the median residual difference of zero.

lation is setup to use the 3D structure up to 30 km depth and a 1D velocity model, similar to the MudPy 1D simulations from 30 km to 200 km depth.

The residuals for the Ibaraki 2011 and Miyagi 2011 earthquake simulations involving 30km-depth 3D structure (3D_30km) and the 200km-depth 3D structures (3D_200km) are consistently lower than residuals from a purely 1D simulations without any 3D structure (Fig. 12). Comparing the two SW4 simulations to the MudPy 1D simulation reveals that the residual values from the 3D_30km simulation are similar to the residuals from the 3D_200km simulation up to a hypocentral distance of about 600 km. However, the residual using the 3D_200km simulation is smaller (i.e., better fit) than the 3D_30km simulation above the 600 km distance. The static displacement residuals are similar at all distances.

This result shows that the reduction of the PGD residuals in the 3D simulations is a combined effect of both shallow and deep 3D structures at hypocentral distances $> \sim 600$ km. Hence, incorporating only the upper 30 km of a 3D structure will still improve the fit to the observed PGD values compared to purely 1D simulations, especially in regions where a deep 3D structure is not available. In other words, the 30km-depth structure plays a role in reducing the PGD residuals, but since the PGD residual compared to the observed waveforms is further reduced in the 3D_200km simulation for larger hypocentral distances, the deeper structure still contributes to the lower residuals. This result is important both in understanding what scale of structure should be included in 3D models, but also in estimating the com-

putational demand in accurately modeling these time series.

4.5 Effect of Maximum Frequency on the Waveform Intensity Measures

Another important question is whether the reduction in the residuals between observed and SW4 3D simulations will persists at higher maximum frequency. To answer the question, we generated 0.50 Hz synthetic waveforms for all the four earthquakes using SW4. We varied the lateral extent of the 3D domain geometry depending on location of each earthquake, thus including fewer stations (Fig. S5), and used one of the 100 ruptures from the FakeQuakes realizations of the mean rupture models to reduce computational cost (Supplementary Material S3). We compared only the intensity measures from the common stations between the 1D and 3D simulations.

For the Ibaraki 2011 earthquakes, we observed similar trends in the PGD, t_{PGD} , SD residuals, and cross correlation values compared to the 0.25 Hz SW4 3D simulation (Fig. 13). However, the median residual difference in the PGD residual compared to the MudPy 1D simulation shows a consistent further reduction in the 0.5 Hz simulation. Hence, even though the overall trend in the residuals persists between the 0.25 Hz and 0.50 Hz simulations, the 0.50 Hz better fits the observed waveforms. Figure 14 shows the PGD residuals for the other earthquakes and rupture models. The figure further validates the reduction in the residual in the 0.50 Hz simulations, except for the Tokachi earthquake (Fig. 14).

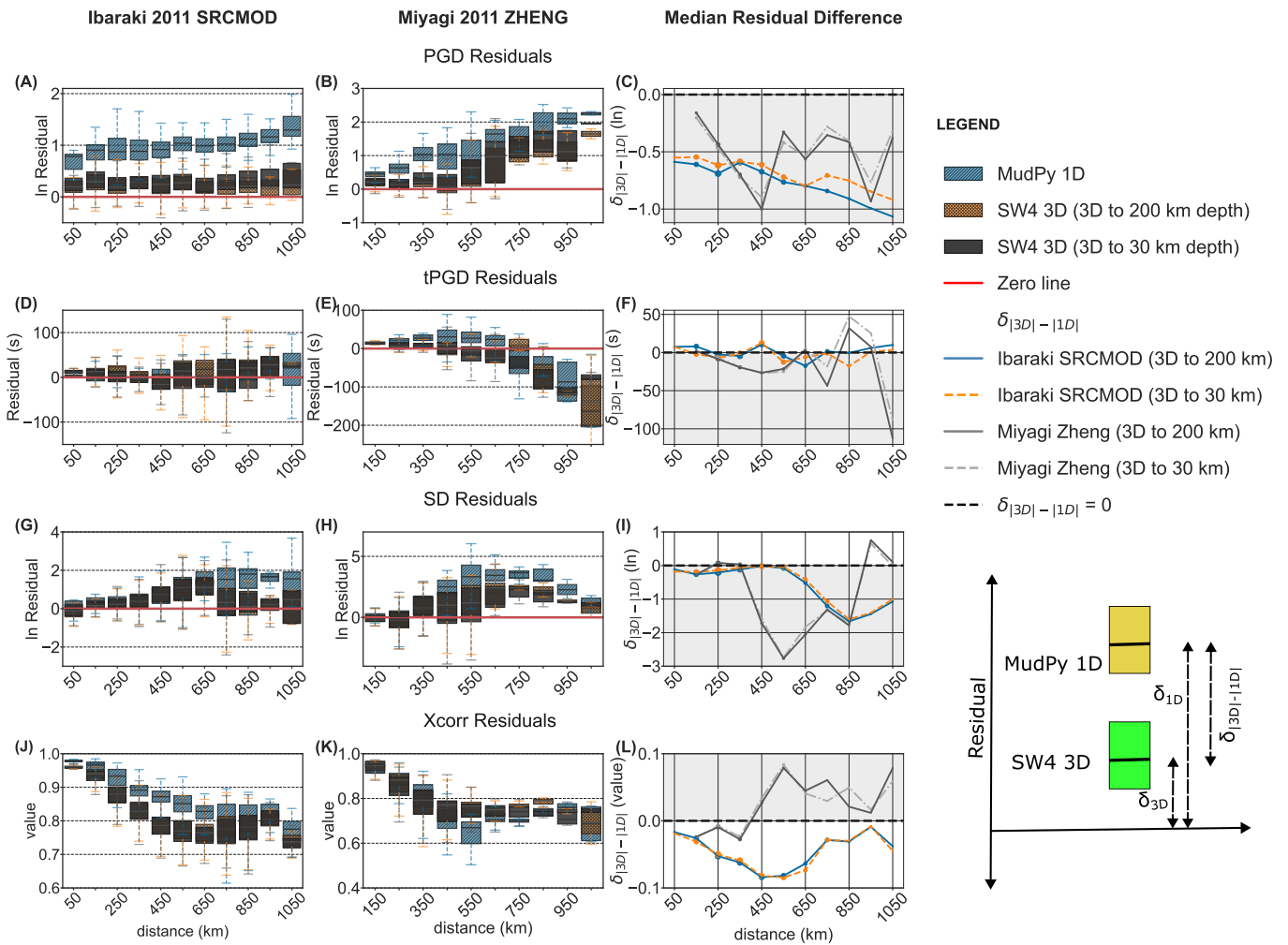


Figure 12 Effect of 3D structure in the upper 0-30 km depth on PGD, t_{PGD} , SD residuals and cross correlation values for Ibaraki 2011 and Miyagi 2011A earthquakes. We compare the MudPy 1D and SW4 3D residuals using 200 km- and 30 km-3D structure at different hypocentral distances. Ibaraki 2011 earthquake is located at 43.2 km depth while Miyagi 2011A earthquake is located at 8.3 km depth, so it is located within the upper 0-30 km depth. The figures on the right column show the median residual difference for the PGD, t_{PGD} , SD residuals and cross correlation values for two simulations compared to the MudPy residuals. Blue boxplots (slant lines hatched style): MudPy 1D residuals; orange boxplots (diamond hatch style): SW4 3D simulation using 200 km-3D structure; gray boxplots (circle hatch style): SW4 3D simulation with 3D structure up to 30 km depth; red horizontal line: zero residual line; blue solid lines: median residual difference for the simulation using the 200 km-3D structure; orange solid line: median residual difference for the 30-km-3D structure; gray shaded regions in left column: regions where “3D fits better than 1D”; white regions represent “1D fits better than 3D”. Bottom right schematic is a visual representation of the meaning of the residuals presented here.

5 Conclusions and Future Work

We present 1D and 3D simulations of four M7.3+ earthquakes in Japan and showed the need to include realistic 3D structure with modern computational approaches and avoid the oversimplification of 1D GNSS models. In the 1D simulations, using different rupture models, PGD residuals do not change significantly with distance for the same earthquake. Therefore, any deviations in the PGD residual for the same rupture model in 3D simulations reveal the effect of the 3D structure. Comparing 1D and 3D residuals, we observed that 3D simulations show improved fits to the observed waveforms, demonstrating that the unmodeled waveform in the 1D simulation is due to the structure (path). However, the observed overall trends in 1D and 3D residuals with distance are likely related to a source model derived with

the assumption of 1D structure or the variation of attenuation parameters within each layer in the 3D structure.

PGD median residuals with distance show that 3D simulations consistently have lower residuals for all simulations, except for Tokachi 2003. The t_{PGD} median residuals are consistently closer to zero for the 3D simulations, generally between 250 km and 700 km distance and up to 1150 km for Iwate 2011 earthquake. The SD median residuals are similar in both 1D and 3D simulations up to about 400 or 500 km, but the 3D simulations fit better at greater distances. The cross-correlation median values are slightly higher in the 3D simulation above hypocentral distance of about 300 km, except for the Ibaraki 2011 earthquake. The K-S tests show that the distributions of the PGD residuals in the 1D and 3D simulations are significantly different for all simulations up to 1000 km distance and 800 km for the Iwate

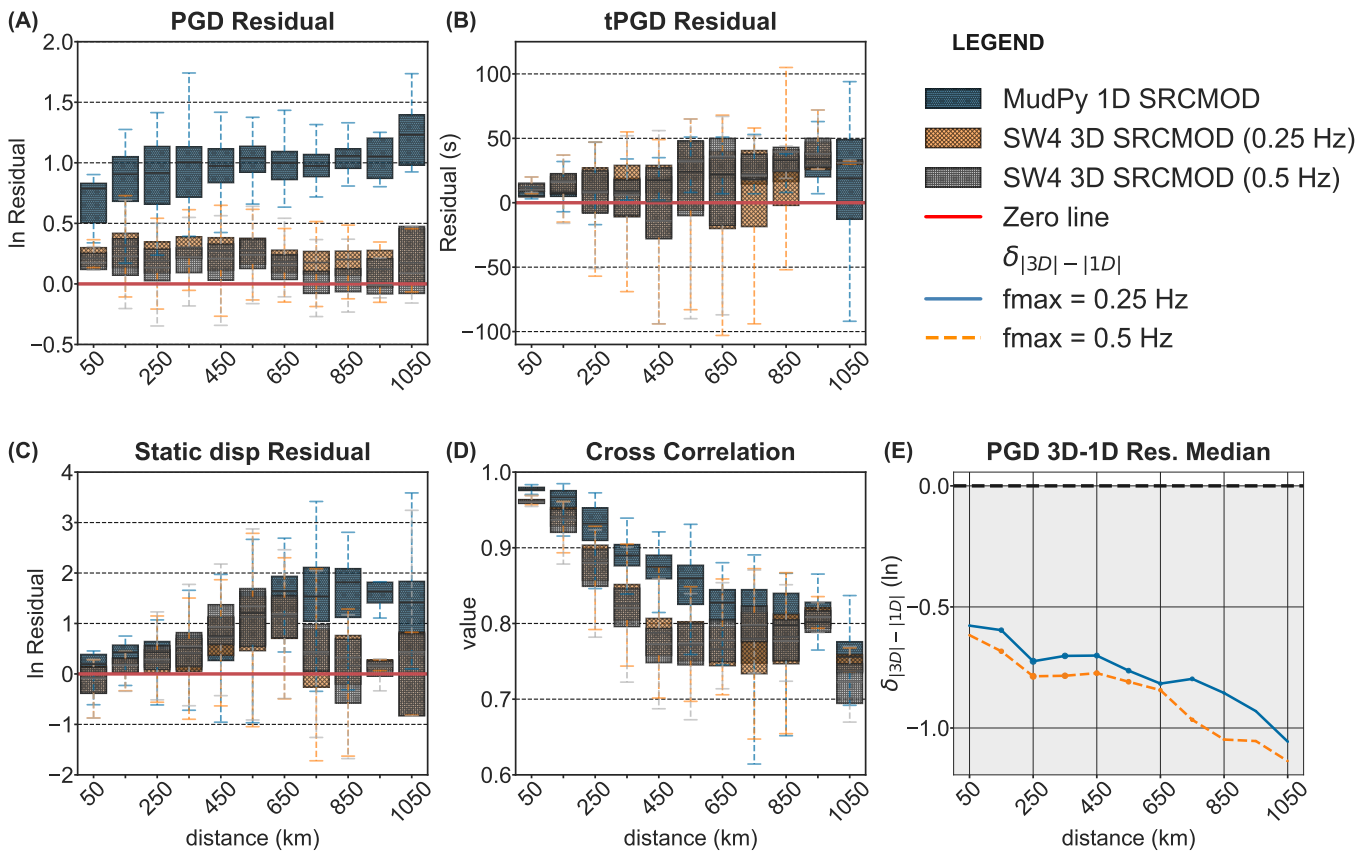


Figure 13 Effect of the maximum frequency (f_{max}) on PGD, t_{PGD} , SD residuals and cross correlation values for Ibaraki 2011 earthquake (using rupture 5 with SRCMOD mean rupture model). Blue boxplots (circle hatched style): MudPy 1D residuals; orange boxplots (diamond hatch style): SW4 3D simulation with f_{max} of 0.25 Hz; gray boxplots (crossed hatched style): SW4 3D simulation with f_{max} of 0.50 Hz; red horizontal line: zero residual line. Figure (E) shows the median residual difference for the PGD residuals compared to the MudPy residuals. Blue solid and orange dash lines represent the median residual difference for the simulation with f_{max} of 0.25 Hz and 0.50 Hz, respectively.

2011 earthquake. The intensity measures for each simulation without considering the variation with distance also show a general reduction in values in the 3D simulations compared to 1D simulations.

This study also shows that the reduction of the PGD residuals in the 3D simulations is a combined effect of both shallow and deep 3D structures especially above certain hypocentral distances. Incorporating only the upper 30 km 3D structure will still improve the fit to the observed PGD values. Lastly, depending on the level of desired model accuracy and available computational resources, the 0.25 Hz SW4 3D simulations may be sufficient to model the kinematics and time-dependent crustal deformation measured by GNSS. Our results demonstrate that future studies of time-dependent crustal deformation should consider using 3D structure or Green’s functions, in particular when peak intensity measures such as PGD are the most critical.

Acknowledgements

This work was funded by NASA ROSES grant 80NSSC21K0841. SW4 simulations were performed on the Lassen graphics processing unit accelerated platform operated by Livermore Computing using a Computing Grand Challenge allocation and on Talapas

High Performance Computing at the University of Oregon. This work was performed in part under the auspices of the U.S. Department of Energy by Lawrence Livermore National Laboratory under Contract DE-AC52-07NA27344. We thank the Computational Infrastructure for Geodynamics (<http://geodynamics.org>) which is funded by the National Science Foundation under awards EAR-0949446 and EAR-1550901. We also appreciate Sui Tung and an anonymous reviewer and editor Mathilde Radiguet for their constructive feedback and suggestions that helped improve the quality of this manuscript.

6 Data and Code Availability

SW4 is an open-source code and available at <https://github.com/geodynamics/sw4> (last accessed January 2023) hosted by the Computational Infrastructure for Geodynamics (<http://geodynamics.org>). MudPy and FakeQuakes are available at <https://github.com/oluwaseunfadugba/MudPy>. Our maps were made with PyGMT (Uieda et al., 2021) available at <https://github.com/GenericMappingTools/pygmt>. PyGMT wraps around GMT6 (Wessel et al., 2019). We used the Slab2.0 model (Hayes, 2018) to create a fault geometry mesh for the Japan Trench using Gmsh (Geuzaine and Remacle, 2009). Our figures were

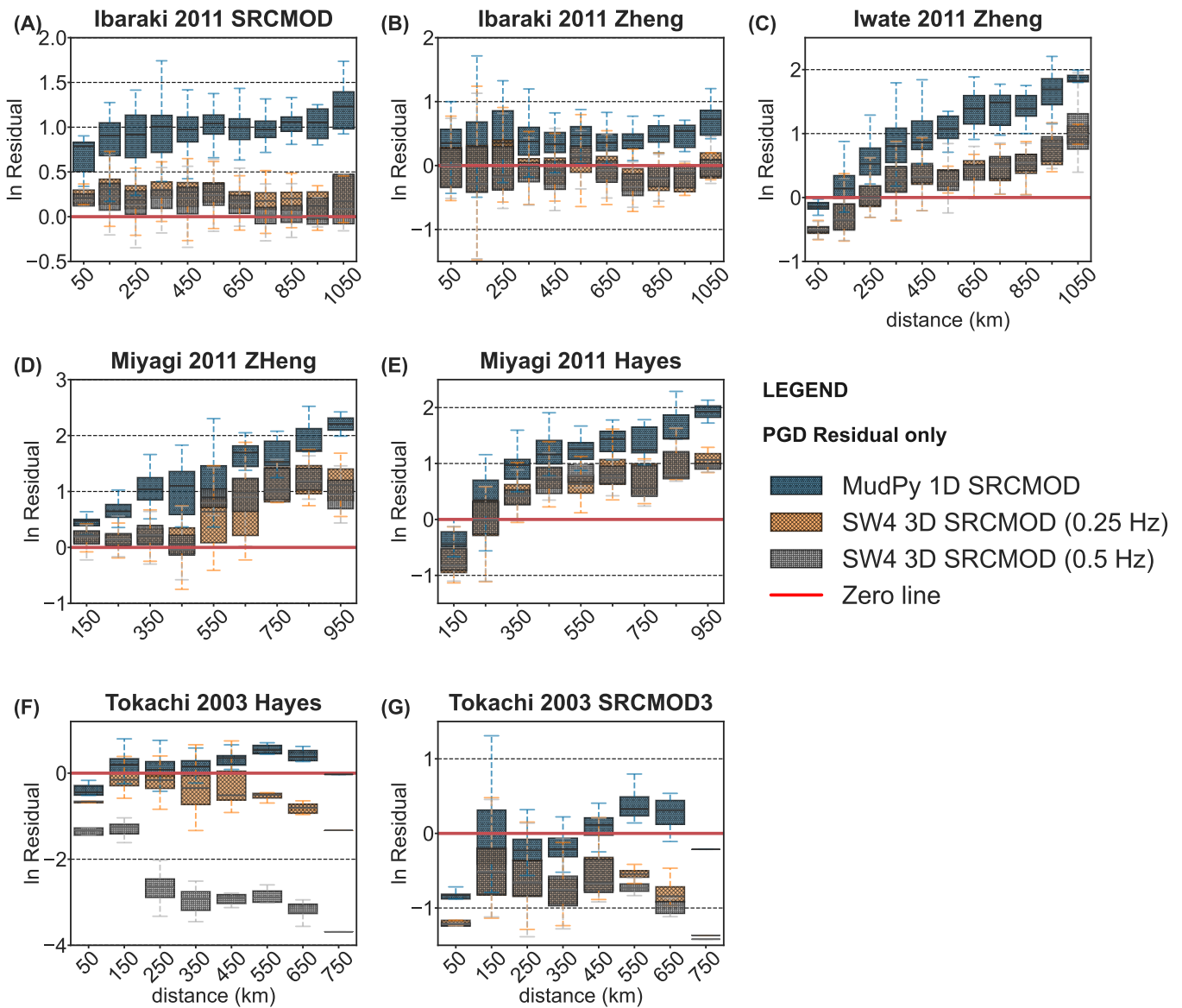


Figure 14 Effect of the maximum frequency (f_{max}) on PGD for all the simulations. The blue boxplots (circle hatched style) represent the MudPy 1D residuals. The orange boxplots (diamond hatch style) represent the SW4 3D simulation with f_{max} of 0.25 Hz. The gray boxplots (crossed hatched style) represent the SW4 3D simulation with f_{max} of 0.50 Hz. The red horizontal line represents the zero residual line.

made with Python 3 (Van Rossum and Drake, 2009), Seaborn (Waskom, 2021), Pandas (McKinney, 2010), and ObsPy (Beyreuther et al., 2010). Our codes are available at https://github.com/oluwaseunfadugba/1D_vs_3D_HR-GNSS_CrustalDeformation. We downloaded the JIVSM (Koketsu et al., 2008, 2009), which is the basis for our 3D modeling, from the Headquarters for Earthquake Research Promotion of Japanese Government (https://www.jishin.go.jp/evaluation/seismic_hazard_map/lpshm/) on 10/14/2021 in two overlapping sections: West Japan (https://www.jishin.go.jp/main/chousa/12_choshuki/dat/nankai/lp2012nankai-w_str.zip) and East Japan (https://www.jishin.go.jp/main/chousa/12_choshuki/dat/nankai/lp2012nankai-e_str.zip), each comprises 23 layers. The physical property values of the layers are from https://www.jishin.go.jp/main/chousa/12_choshuki/dat/nankai/lp2012nankai_str_val.pdf. The version provided here is not the original version published by JIVSM and is instead a modified version. The

GNSS stations, mesh, 3D velocity model, projected rupture models for each earthquake on the Japan Trench mesh, the codes at the time of publication and the corresponding 100 realizations of the mean rupture models generated using FakeQuakes are available on Zenodo (Fadugba et al., 2023).

7 Competing Interests

The authors have no competing interests.

References

Aagaard, B. T., Knepley, M. G., and Williams, C. A. A domain decomposition approach to implementing fault slip in finite-element models of quasi-static and dynamic crustal deformation. *Journal of Geophysical Research: Solid Earth*, 118(6): 3059–3079, June 2013. doi: 10.1002/jgrb.50217.

- Baltay, A. S., Hanks, T. C., and Abrahamson, N. A. Uncertainty, Variability, and Earthquake Physics in Ground-Motion Prediction Equations. *Bulletin of the Seismological Society of America*, May 2017. doi: 10.1785/0120160164.
- Beyreuther, M., Barsch, R., Krischer, L., Megies, T., Behr, Y., and Wassermann, J. ObsPy: A Python Toolbox for Seismology. *Seismological Research Letters*, 81(3):530–533, May 2010. doi: 10.1785/gssrl.81.3.530.
- Blaser, L., Kruger, F., Ohrnberger, M., and Scherbaum, F. Scaling Relations of Earthquake Source Parameter Estimates with Special Focus on Subduction Environment. *Bulletin of the Seismological Society of America*, 100(6):2914–2926, Dec. 2010. doi: 10.1785/0120100111.
- Bock, Y., Melgar, D., and Crowell, B. W. Real-Time Strong-Motion Broadband Displacements from Collocated GPS and Accelerometers. *Bulletin of the Seismological Society of America*, 101(6):2904–2925, Dec. 2011. doi: 10.1785/0120110007.
- Delouis, B., Nocquet, J., and Vallée, M. Slip distribution of the February 27, 2010 Mw = 8.8 Maule Earthquake, central Chile, from static and high-rate GPS, InSAR, and broadband teleseismic data. *Geophysical Research Letters*, 37(17), Sept. 2010. doi: 10.1029/2010gl043899.
- Dziewonski, A. M. and Anderson, D. L. Preliminary reference Earth model. *Physics of the Earth and Planetary Interiors*, 25(4): 297–356, June 1981. doi: 10.1016/0031-9201(81)90046-7.
- Fadugba, O. I., Sahakian, V. J., Melgar, D. M., Rodgers, A., and Shimony, R. The Impact of the Three-Dimensional Structure of a Subduction Zone on Time-dependent Crustal Deformation Measured by HR-GNSS, 2023. doi: 10.5281/zenodo.7765170.
- Furumura, T. and Kennett, B. L. N. On the nature of regional seismic phases-III. The influence of crustal heterogeneity on the wavefield for subduction earthquakes: the 1985 Michoacan and 1995 Copala, Guerrero, Mexico earthquakes. *Geophysical Journal International*, 135(3):1060–1084, Dec. 1998. doi: 10.1046/j.1365-246x.1998.00698.x.
- Furumura, T. and Kennett, B. L. N. Subduction zone guided waves and the heterogeneity structure of the subducted plate: Intensity anomalies in northern Japan. *Journal of Geophysical Research: Solid Earth*, 110(B10), Oct. 2005. doi: 10.1029/2004jb003486.
- Furumura, T. and Singh, S. Regional Wave Propagation from Mexican Subduction Zone Earthquakes: The Attenuation Functions for Interplate and Inslab Events. *Bulletin of the Seismological Society of America*, 92(6):2110–2125, Aug. 2002. doi: 10.1785/0120010278.
- Geng, J., Pan, Y., Li, X., Guo, J., Liu, J., Chen, X., and Zhang, Y. Noise Characteristics of High-Rate Multi-GNSS for Subdaily Crustal Deformation Monitoring. *Journal of Geophysical Research: Solid Earth*, 123(2):1987–2002, Feb. 2018. doi: 10.1002/2018jb015527.
- Geuzaine, C. and Remacle, J. Gmsh: A 3-D finite element mesh generator with built-in pre- and post-processing facilities. *International Journal for Numerical Methods in Engineering*, 79(11): 1309–1331, May 2009. doi: 10.1002/nme.2579.
- Goldberg, D., Melgar, D., Hayes, G., Crowell, B., and Sahakian, V. A Ground-Motion Model for GNSS Peak Ground Displacement. *Bulletin of the Seismological Society of America*, 111, 2021. doi: 10.1785/0120210042.
- Goldberg, D. E. and Melgar, D. Generation and Validation of Broadband Synthetic P Waves in Semistochastic Models of Large Earthquakes. *Bulletin of the Seismological Society of America*, 110(4):1982–1995, July 2020. doi: 10.1785/0120200049.
- Goldberg, D. E., Koch, P., Melgar, D., Riquelme, S., and Yeck, W. L. Beyond the Teleseism: Introducing Regional Seismic and Geodetic Data into Routine USGS Finite-Fault Modeling. *Seismological Research Letters*, 93(6):3308–3323, Aug. 2022. doi: 10.1785/0220220047.
- Graves, R. Standard Rupture Format Version 2.0, 2014.
- Graves, R. and Pitarka, A. Refinements to the Graves and Pitarka (2010) Broadband Ground-Motion Simulation Method. *Seismological Research Letters*, 86(1):75–80, Dec. 2014. doi: 10.1785/0220140101.
- Graves, R. W. and Pitarka, A. Broadband Ground-Motion Simulation Using a Hybrid Approach. *Bulletin of the Seismological Society of America*, 100(5A):2095–2123, Sept. 2010. doi: 10.1785/0120100057.
- Hartzell, S., Harmsen, S., and Frankel, A. Effects of 3D Random Correlated Velocity Perturbations on Predicted Ground Motions. *Bulletin of the Seismological Society of America*, 100(4):1415–1426, July 2010. doi: 10.1785/0120090060.
- Hayes, G. Slab2 - A Comprehensive Subduction Zone Geometry Model, 2018. doi: 10.5066/F7PV6JNV.
- Hayes, G. P. The finite, kinematic rupture properties of great-sized earthquakes since 1990. *Earth and Planetary Science Letters*, 468:94–100, June 2017. doi: 10.1016/j.epsl.2017.04.003.
- Hearn, E. and Burgmann, R. The Effect of Elastic Layering on Inversions of GPS Data for Coseismic Slip and Resulting Stress Changes: Strike-Slip Earthquakes. *Bulletin of the Seismological Society of America*, 95(5):1637–1653, Oct. 2005. doi: 10.1785/0120040158.
- Ide, S. *Slip Inversion*, page 193–223. Elsevier, 2007. doi: 10.1016/b978-044452748-6.00068-7.
- Kaneko, Y., Ito, Y., Chow, B., Wallace, L. M., Tape, C., Grapenthin, R., D’Anastasio, E., Henrys, S., and Hino, R. Ultra-long Duration of Seismic Ground Motion Arising From a Thick, Low-Velocity Sedimentary Wedge. *Journal of Geophysical Research: Solid Earth*, 124(10):10347–10359, Oct. 2019. doi: 10.1029/2019jb017795.
- Koketsu, K., Hikima, K., Miyazaki, S., and Ide, S. Joint inversion of strong motion and geodetic data for the source process of the 2003 Tokachi-oki, Hokkaido, earthquake. *Earth, Planets and Space*, 56(3):329–334, 2004. doi: 10.1186/bf03353060.
- Koketsu, K., Miyake, H., Fujiwara, H., and Hashimoto, H. Progress towards a Japan integrated velocity structure model and long-period ground motion hazard map,. *Proceedings of the 14th World Conference on Earthquake Engineering, Paper*, 2008.
- Koketsu, K., Miyake, H., Afnimar, and Tanaka, Y. A proposal for a standard procedure of modeling 3-D velocity structures and its application to the Tokyo metropolitan area, Japan. *Tectonophysics*, 472(1–4):290–300, July 2009. doi: 10.1016/j.tecto.2008.05.037.
- Kolmogorov, A. Sulla determinazione empirica di una legge di distribuzione. *Giornale dell’Istituto Italiano degli Attuari*, 4:83–91 5, 1933.
- Kotha, S. R., Weatherill, G., Bindi, D., and Cotton, F. A regionally-adaptable ground-motion model for shallow crustal earthquakes in Europe. *Bulletin of Earthquake Engineering*, 18(9): 4091–4125, May 2020. doi: 10.1007/s10518-020-00869-1.
- Kubo, H., Asano, K., and Iwata, T. Source-rupture process of the 2011 Ibaraki-oki, Japan, earthquake (Mw 7.9) estimated from the joint inversion of strong-motion and GPS Data: Relationship with seamount and Philippine Sea Plate. *Geophysical Research Letters*, 40(12):3003–3007, June 2013. doi: 10.1002/grl.50558.
- Kuehn, N. M. and Abrahamson, N. A. Spatial correlations of ground motion for non-ergodic seismic hazard analysis. *Earthquake Engineering & Structural Dynamics*, 49(1):4–23, Oct. 2019. doi: 10.1002/eqe.3221.
- Landwehr, N., Kuehn, N. M., Scheffer, T., and Abrahamson, N. A Nonergodic Ground-Motion Model for California with

- Spatially Varying Coefficients. *Bulletin of the Seismological Society of America*, 106(6):2574–2583, Oct. 2016. doi: 10.1785/0120160118.
- Langer, L., Gharti, H. N., and Tromp, J. Impact of topography and three-dimensional heterogeneity on coseismic deformation. *Geophysical Journal International*, 217(2):866–878, Jan. 2019. doi: 10.1093/gji/ggz060.
- Langer, L., Beller, S., Hirakawa, E., and Tromp, J. Impact of sedimentary basins on Green's functions for static slip inversion. *Geophysical Journal International*, 232(1):569–580, Aug. 2022. doi: 10.1093/gji/ggac344.
- Laske, G., Masters, G., Ma, Z., and Pasyanos, M. Update on CRUST1.0 — A 1-degree global model of Earth's crust. *Geophysical research abstracts*, 15(15):2658, 2013.
- LeVeque, R. J., Waagan, K., González, F. I., Rim, D., and Lin, G. Generating Random Earthquake Events for Probabilistic Tsunami Hazard Assessment. *Pure and Applied Geophysics*, 173(12): 3671–3692, Aug. 2016. doi: 10.1007/s00024-016-1357-1.
- Maeda, T., Takemura, S., and Furumura, T. OpenSWPC: an open-source integrated parallel simulation code for modeling seismic wave propagation in 3D heterogeneous viscoelastic media. *Earth, Planets and Space*, 69(1), July 2017. doi: 10.1186/s40623-017-0687-2.
- Mann, M. E. and Abers, G. A. First-Order Mantle Subduction-Zone Structure Effects on Ground Motion: The 2016 Mw 7.1 Iniskin and 2018 Mw 7.1 Anchorage Earthquakes. *Seismological Research Letters*, 91(1):85–93, Oct. 2019. doi: 10.1785/0220190197.
- McKinney, W. Data Structures for Statistical Computing in Python. In *Proceedings of the 9th Python in Science Conference*, SciPy, SciPy, 2010. doi: 10.25080/majora-92bf1922-00a.
- Melgar, D. and Bock, Y. Kinematic earthquake source inversion and tsunami runup prediction with regional geophysical data. *Journal of Geophysical Research: Solid Earth*, 120(5):3324–3349, May 2015. doi: 10.1002/2014jb011832.
- Melgar, D. and Hayes, G. P. Characterizing large earthquakes before rupture is complete. *Science Advances*, 5(5), May 2019. doi: 10.1126/sciadv.aav2032.
- Melgar, D., LeVeque, R. J., Dreger, D. S., and Allen, R. M. Kinematic rupture scenarios and synthetic displacement data: An example application to the Cascadia subduction zone. *Journal of Geophysical Research: Solid Earth*, 121(9):6658–6674, Sept. 2016. doi: 10.1002/2016jb013314.
- Melgar, D., Crowell, B. W., Melbourne, T. I., Szeliga, W., Santillan, M., and Scrivner, C. Noise Characteristics of Operational Real-Time High-Rate GNSS Positions in a Large Aperture Network. *Journal of Geophysical Research: Solid Earth*, 125(7), June 2020a. doi: 10.1029/2019jb019197.
- Melgar, D., Ganas, A., Taymaz, T., Valkaniotis, S., Crowell, B. W., Kapetanidis, V., Tsironi, V., Yolsal-Çevikbilen, S., and Öcalan, T. Rupture kinematics of 2020 January 24 Mw 6.7 Doğanyol-Sivrice, Turkey earthquake on the East Anatolian Fault Zone imaged by space geodesy. *Geophysical Journal International*, 223(2):862–874, July 2020b. doi: 10.1093/gji/ggaa345.
- Mena, B., Mai, P. M., Olsen, K. B., Purvance, M. D., and Brune, J. N. Hybrid Broadband Ground-Motion Simulation Using Scattering Green's Functions: Application to Large-Magnitude Events. *Bulletin of the Seismological Society of America*, 100(5A):2143–2162, Sept. 2010. doi: 10.1785/0120080318.
- N.O.A.A. National Geophysical Data Center. ETOPO1 1 Arc-Minute Global Relief Model, 2009. Accessed [10/14/2021].
- Olsen, K. B. Site Amplification in the Los Angeles Basin from Three-Dimensional Modeling of Ground Motion. *Bulletin of the Seismological Society of America*, 90(6B):S77–S94, Dec. 2000. doi: 10.1785/0120000506.
- Ozawa, S., Nishimura, T., Suito, H., Kobayashi, T., Tobita, M., and Imakiire, T. Coseismic and postseismic slip of the 2011 magnitude-9 Tohoku-Oki earthquake. *Nature*, 475(7356): 373–376, June 2011. doi: 10.1038/nature10227.
- Petersson, N. A. and Sjögreen, B. Stable and Efficient Modeling of Anelastic Attenuation in Seismic Wave Propagation. *Communications in Computational Physics*, 12(1):193–225, July 2012. doi: 10.4208/cicp.201010.090611a.
- Petersson, N. A. and Sjögreen, B. Wave propagation in anisotropic elastic materials and curvilinear coordinates using a summation-by-parts finite difference method. *Journal of Computational Physics*, 299:820–841, Oct. 2015. doi: 10.1016/j.jcp.2015.07.023.
- Petersson, N. A. and Sjögreen, B. geodynamics/sw4: SW4, version 2.01, 2017. doi: 10.5281/ZENODO.1063644.
- Rodgers, A. J., Anders Petersson, N., Pitarka, A., McCallen, D. B., Sjögreen, B., and Abrahamson, N. Broadband (0–5 Hz) Fully Deterministic 3D Ground-Motion Simulations of a Magnitude 7.0 Hayward Fault Earthquake: Comparison with Empirical Ground-Motion Models and 3D Path and Site Effects from Source Normalized Intensities. *Seismological Research Letters*, 90(3): 1268–1284, Feb. 2019. doi: 10.1785/0220180261.
- Rodgers, A. J., Pitarka, A., Pankajakshan, R., Sjögreen, B., and Petersson, N. A. Regional-Scale 3D Ground-Motion Simulations of Mw 7 Earthquakes on the Hayward Fault, Northern California Resolving Frequencies 0–10 Hz and Including Site-Response Corrections. *Bulletin of the Seismological Society of America*, 110(6):2862–2881, Aug. 2020. doi: 10.1785/0120200147.
- Ruhl, C. J., Melgar, D., Geng, J., Goldberg, D. E., Crowell, B. W., Allen, R. M., Bock, Y., Barrientos, S., Riquelme, S., Baez, J. C., Cabral-Cano, E., Pérez-Campos, X., Hill, E. M., Protti, M., Ganas, A., Ruiz, M., Mothes, P., Jarrín, P., Nocquet, J., Avouac, J., and D'Anastasio, E. A Global Database of Strong-Motion Displacement GNSS Recordings and an Example Application to PGD Scaling. *Seismological Research Letters*, 90(1):271–279, Oct. 2018. doi: 10.1785/0220180177.
- Sahakian, V., Melgar, D., and Muzli, M. Weak Near-Field Behavior of a Tsunami Earthquake: Toward Real-Time Identification for Local Warning. *Geophysical Research Letters*, 46(16):9519–9528, Aug. 2019a. doi: 10.1029/2019gl083989.
- Sahakian, V. J., Melgar, D., Quintanar, L., Ramírez-Guzmán, L., Pérez-Campos, X., and Baltay, A. Ground Motions from the 7 and 19 September 2017 Tehuantepec and Puebla-Morelos, Mexico, Earthquakes. *Bulletin of the Seismological Society of America*, Oct. 2018. doi: 10.1785/0120180108.
- Sahakian, V. J., Baltay, A., Hanks, T. C., Buehler, J., Vernon, F. L., Kilb, D., and Abrahamson, N. A. Ground Motion Residuals, Path Effects, and Crustal Properties: A Pilot Study in Southern California. *Journal of Geophysical Research: Solid Earth*, 124(6): 5738–5753, June 2019b. doi: 10.1029/2018jb016796.
- Sjögreen, B. and Petersson, N. A. A Fourth Order Accurate Finite Difference Scheme for the Elastic Wave Equation in Second Order Formulation. *Journal of Scientific Computing*, 52(1):17–48, Sept. 2011. doi: 10.1007/s10915-011-9531-1.
- Smirnov, N. Table for Estimating the Goodness of Fit of Empirical Distributions. *The Annals of Mathematical Statistics*, 19(2): 279–281, June 1948. doi: 10.1214/aoms/1177730256.
- Tung, S. and Masterlark, T. Sensitivities of Near-field Tsunami Forecasts to Megathrust Deformation Predictions. *Journal of Geophysical Research: Solid Earth*, 123(2):1711–1735, Feb. 2018. doi: 10.1002/2017jb015354.
- Ueno, H., Hatakeyama, S., Aketagawa, T., Funasaki, J., and

- Hamada, N. Improvement of hypocenter determination procedures in the Japan Meteorological Agency. *Quarterly Journal of Seismology*, 65:123 – 134, 2002.
- Uieda, L., Tian, D., Leong, W. J., Toney, L., Schlitzer, W., Yao, J., Grund, M., Jones, M., Materna, K., Newton, T., Ziebarth, M., and Wessel, P. PyGMT: A Python interface for the Generic Mapping Tools, 2021. doi: 10.5281/ZENODO.4592991.
- Van Rossum, G. and Drake, F. *Python 3 Reference Manual*. CreateSpace, Scotts Valley, CA, 2009.
- Vidale, J. and Helmberger, D. Elastic finite-difference modeling of the 1971 San Fernando, California earthquake. *Bulletin of the Seismological Society of America*, 78(1):122–141, 1988. doi: 10.1785/BSSA0780010122.
- Wald, D. J. and Graves, R. W. Resolution analysis of finite fault source inversion using one- and three-dimensional Green's functions: 2. Combining seismic and geodetic data. *Journal of Geophysical Research: Solid Earth*, 106(B5):8767–8788, May 2001. doi: 10.1029/2000jb900435.
- Wallace, L. M., Kaneko, Y., Hreinsdóttir, S., Hamling, I., Peng, Z., Bartlow, N., D'Anastasio, E., and Fry, B. Large-scale dynamic triggering of shallow slow slip enhanced by overlying sedimentary wedge. *Nature Geoscience*, 10(10):765–770, Sept. 2017. doi: 10.1038/ngeo3021.
- Waskom, M. seaborn: statistical data visualization. *Journal of Open Source Software*, 6(60):3021, Apr. 2021. doi: 10.21105/joss.03021.
- Wessel, P., Luis, J. F., Uieda, L., Scharroo, R., Wobbe, F., Smith, W. H. F., and Tian, D. The Generic Mapping Tools Version 6. *Geochemistry, Geophysics, Geosystems*, 20(11):5556–5564, Nov. 2019. doi: 10.1029/2019gc008515.
- Williams, C. A. and Wallace, L. M. Effects of material property variations on slip estimates for subduction interface slow-slip events. *Geophysical Research Letters*, 42(4):1113–1121, Feb. 2015. doi: 10.1002/2014gl062505.
- Wirth, E. A., Sahakian, V. J., Wallace, L. M., and Melnick, D. The occurrence and hazards of great subduction zone earthquakes. *Nature Reviews Earth & Environment*, 3(2):125–140, Jan. 2022. doi: 10.1038/s43017-021-00245-w.
- Yagi, Y. Source rupture process of the 2003 Tokachi-oki earthquake determined by joint inversion of teleseismic body wave and strong ground motion data. *Earth, Planets and Space*, 56(3):311–316, 2004. doi: 10.1186/bf03353057.
- Yamanaka, Y. and Kikuchi, M. Source process of the recurrent Tokachi-oki earthquake on September 26, 2003, inferred from teleseismic body waves. *Earth, Planets and Space*, 55(12):e21–e24, 2003. doi: 10.1186/bf03352479.
- Yue, H. and Lay, T. Inversion of high-rate (1 sps) GPS data for rupture process of the 11 March 2011 Tohoku earthquake (Mw 9.1). *Geophysical Research Letters*, 38(7), Apr. 2011. doi: 10.1029/2011gl048700.
- Zhang, H., Melgar, D., Sahakian, V., Searcy, J., and Lin, J.-T. Learning source, path and site effects: CNN-based on-site intensity prediction for earthquake early warning. *Geophysical Journal International*, 231(3):2186–2204, Aug. 2022. doi: 10.1093/gji/ggac325.
- Zheng, X., Zhang, Y., Wang, R., Zhao, L., Li, W., and Huang, Q. Automatic Inversions of Strong-Motion Records for Finite-Fault Models of Significant Earthquakes in and Around Japan. *Journal of Geophysical Research: Solid Earth*, 125(9), Sept. 2020. doi: 10.1029/2020jb019992.
- Zhu, L. and Rivera, L. A. A note on the dynamic and static displacements from a point source in multilayered media. *Geophysical Journal International*, 148(3):619–627, Mar. 2002. doi: 10.1046/j.1365-246x.2002.01610.x.

The article *The Impact of the Three-Dimensional Structure of a Subduction Zone on Time-dependent Crustal Deformation Measured by HR-GNSS* © 2024 by Oluwaseun Idowu Fadugba is licensed under CC BY 4.0.